Depletion of rRNA Methyltranferase METTL5 Enhances Anti-Tumor Immune Response via Neoantigen Generated from Cryptic Translation

Yangyi Zhang[1, #], Xiaoyan Shi[1, #], Yuci Wang[1, #], Ruiqi Wang[1], Folan Lin[2, 3], Yanlan Cao[1], Wanqiu Li[2, 3, *], Hao Chen[1, *]

[1]Department of Human Cell Biology and Genetics, SUSTech Homeostatic Medicine Institute, Joint Laboratory of Guangdong & Hong Kong Universities for Vascular Homeostasis and Diseases, School of Medicine, Southern University of Science and Technology, Shenzhen 518055, China.

[2]Department of Pharmacology, SUSTech Homeostatic Medicine Institute, Joint Laboratory of Guangdong-Hong Kong Universities for Vascular Homeostasis and Diseases, School of Medicine, Southern University of Science and Technology, Shenzhen 518055, China

[3]Institute for Biological Electron Microscopy, Southern University of Science and Technology, Shenzhen, 518055, China

[#]These authors contributed equally to this work.

[*]Corresponding authors: liwq3@sustech.edu.cn (W.Q.L.); chenh7@sustech.edu.cn (H.C.).

ABSTRACT

Tumor neoantigens play a pivotal role in eliciting tumor-specific immune responses and holds the promise for personalized immunotherapy. However, previous studies mainly focused on the tumor-specific neoantigens derived from genomic mutation and aberrant RNA splicing, limiting the repertoire of targetable neoantigens. Here, we demonstrate that inhibition of rRNA methyltransferase METTL5 translationally increases neoantigen production and enhances anti-tumor immunity. Mechanistically, METTL5-mediated m^6A modification at the decoding center of small ribosomal subunit maintains the proper function of ribosome during mRNA translation. *METTL5*-deficiency decreases translation fidelity and increases production of tumor cell-specific antigens derived from non-canonical translation. Furthermore, we found that *Mettl5*-depletion increased $CD8^+$T cell infiltration density and T cell receptor (TCR) repertoire diversity in murine tumor models. Importantly, this immunostimulatory effect strictly depended on intact antigen presentation pathways, suggesting that *Mettl5* knockout exerts its effects primarily through neoantigen generation. Together, this study uncovers the intrinsic mechanisms sustaining mRNA translation accuracy, elucidates a novel source of tumor neoantigen generation, and proposes a new strategy to enhance immunotherapy through targeting mRNA translation.

INTRODUCTION

The complexity of cancer therapy originates from the high heterogeneity of tumors, dynamic immune escape mechanisms, and the multi-faceted challenges posed by the immunosuppressive tumor microenvironment[1-8]. Conventional therapies (e.g., chemotherapy and radiotherapy) often cause severe toxic side effects with limited therapeutic efficacy, whereas immunotherapy, despite its advantages of low toxicity and durable responses, remains constrained by low response rates and the development of acquired resistance[3-5,9-16].

A promising solution lies in the identification of tumor-specific mutations to generate neoantigens, which can activate polyclonal T-cell responses, overcome immune tolerance, and avoid off-target toxicity[17-24]. This "dynamic targeting" approach offers a means to address heterogeneity and drug resistance[4,5,25,26]. Neoantigens, derived from short peptides (8–25 amino acids) resulting from errors in gene expression regulation, are presented on tumor cell surfaces by human leukocyte antigen (HLA) molecules, enabling T-cell recognition[27-30]. Unlike self-antigens, neoantigens are not subject to central tolerance mechanisms and exhibit robust immunogenicity, making them ideal targets for immunotherapy[17,18,21,23,31-33].

Certain tumor mutations had been found to enhance the quality and quantity of functional neoantigens, such as those targeting highly immunogenic mutations like KRAS G12D, IDH1 R132H, and TP53[34-37]. These neoantigen vaccines have demonstrated the ability to activate T-cell responses in solid tumors such as pancreatic cancer and even penetrate the blood-brain barrier in glioma[38,39]. Furthermore, the combination of personalized vaccines (e.g., NeoVax) with immune checkpoint inhibitors has advanced clinical exploration in precision immunotherapy, suggesting that the quality of neoantigens generated by tumor mutations may guide therapeutic efficacy[40].

Despite recent advances in tumor neoantigen, clinical application of neoantigen-targeted therapies faces multiple challenges. First, most antigens arising from tumor mutations are of low quality (e.g., synonymous mutations or cryptic epitopes), exhibiting insufficient immunogenicity[41-45]. Second, certain mutated peptides share high sequence homology with self-proteins, leading to weakened anti-tumor immune responses due to central tolerance (thymic selection) or peripheral tolerance (T cell exhaustion) mechanisms[16,46]. More critically, the process of immune editing within the tumor microenvironment continuously eliminates highly immunogenic epitopes, leaving residual antigen pools dominated by low-affinity variants that further impair T cell activation efficiency[43,47]. To overcome these limitations, current intervention strategies-such as CRISPR/Cas9-induced mutations or DNA-damaging agents to enhance neoantigen load, which can transiently expand neoantigen numbers[5,48,49]. However, their irreversible genomic modifications risk exacerbating tumor heterogeneity or causing normal tissue toxicity, significantly hindering clinical application of these approaches[50,51].

To address the critical challenge of limited availability of tumor-specific neoantigens, we explored translational regulation as a reversible and safer strategy to augment neoantigen production. In current study, we integrated multi-omics analysis with functional validation to demonstrate that loss of METTL5-mediated m^6A modification in ribosomes induces neoantigen generation through disrupting translational fidelity. The neoantigens derived from mistranslation significantly diversified the T cell receptor (TCR) repertoire and enhanced $CD8^+$ T cell infiltration. Our findings expand both the diversity and sources of tumor neoantigens, offering a novel pathway to enhance anti-tumor immune responses.

RESULTS

METTL5 is identified as a negative regulator of tumor immunogenicity

To identify the chemical modifications of ribosomal RNA that relate with resistance to immunotherapy, we systematically compared the differential expression profiles of 11 key rRNA modifiers between responders (n=82) and non-responders (n=72) of ICI (Immune-checkpoint inhibitors)-treated samples[52](Fig. 1A). Notably, the result revealed that the expression level of METTL5 is negatively associated with immunotherapy responses (Fig. 1A). Previous studies demonstrated that METTL5 must form a heterodimeric complex with TRMT112 to functionally catalyze m^6A methylation of adenosine at position 1832 in 18S rRNA[53-55]. Interestingly, elevated TRMT112 expression also serves as a negative predictor of immunotherapy response, which suggests that 18S rRNA m^6A modification mediated by METTL5-TRMT112 may be intrinsically linked to tumor immunity.

To evaluate the regulatory role of METTL5 in tumor immunogenicity, we generated *Mettl5*-knockout B16-F10 melanoma and 4T1 breast cancer cell lines using CRISPR/Cas9-mediated gene editing (Fig. S1A). Sanger sequencing confirmed biallelic frameshift mutations at the *Mettl5* locus, with indel events clustered around the gRNA target site (Fig. S1A). Quantitative Reverse Transcription PCR (RT-qPCR) demonstrated significant transcript depletion (>70%) in both *Mettl5*-KO cell lines (Fig. S1B). Consistently, high-performance liquid chromatography-mass spectrometry (HPLC-MS) quantification revealed significant decrease of m^6A modification in *Mettl5*-KO cells (Fig. S1C). Furthermore, cell growth assays showed no significant differences between *Mettl5*-KO and scrambled (SCR) control in either cell line (Fig. 1B). Similarly, clonogenic survival assays demonstrated comparable colony-forming abilities (Fig. S1D, S1E). These findings suggest that the loss of *Mettl5* does not significantly impair the proliferation capacity of tumor cells *in vitro*.

119 Then we established syngeneic tumor models to determine the immunological
120 consequences of *Mettl5* depletion using immunocompromised (nude) and
121 immunocompetent (C57BL/6N or Balb/c) mice, respectively. Consistent with the *in*
122 *vitro* results, *Mettl5* loss did not influence the ability of B16-F10 cells to form tumors
123 in nude mice with deficient immune systems (Fig. 1C). In contrast, when *Mettl5*-
124 deficient cells were inoculated into syngeneic mouse hosts, their abilities to form
125 tumors were significantly attenuated compared with control cells (Fig. 1D, E). To more
126 precisely assess the role of METTL5 in tumor immunity, we carried out competitive
127 cell growth assays to compare the proliferation rates of GFP-labeled *Mettl5*-KO and
128 mCherry-labeled SCR B16-F10 cells under identical conditions. Consistently, the
129 results demonstrated that *Mettl5*-deficient cells only exhibited growth suppression
130 compared to control cells in immunocompetent mice (Fig. 1F-H). Collectively, these
131 findings demonstrate that METTL5 regulates tumor growth through an immune-
132 dependent mechanism.
133
134 ***Mettl5* knockout promotes immune cell infiltration in tumor**
135 To elucidate how *Mettl5* depletion suppresses tumor growth specifically in
136 immunocompetent hosts, we systematically characterized immune cell dynamics
137 within the tumor microenvironment (TME). Immunohistochemical (IHC) analysis of
138 B16-F10 and 4T1 tumors revealed significantly enhanced $CD8^+$ T cell infiltration in
139 *Mettl5*-KO tumor model compared to SCR control (Fig. 2A, B). To quantitatively
140 profile immune populations, we isolated leukocytes from B16-F10 tumors using Percoll
141 gradient centrifugation for multicolor flow cytometry analysis. *Mettl5*-KO tumors
142 exhibited marked increases in $CD8^+$ T cells, accompanied by elevated proportions of
143 NK cells and TH cells (Fig. 2C, D). These findings were further supported by spleen
144 immunophenotyping, which revealed expanded cytotoxic T lymphocyte (CTL)
145 populations in *Mettl5*-KO tumor-bearing mice (Fig. 2E, F). Lastly, we performed
146 single-cell RNA sequencing (scRNA-seq) to characterize infiltrating lymphocyte

147 populations in freshly isolated tumor tissues (Fig. S2A). Unsupervised clustering
148 identified major immune subsets including $CD8^+$ T cells, B cells, macrophages, and
149 dendritic cells (Fig. S2B-D). Notably, the TMEs of *Mettl5*-KO tumor contained higher
150 proportions of $CD8^+$ T cells compared to controls (4% vs 2.5%) (Fig. S2E). Therefore,
151 scRNA-seq data consistently validated the immunostimulatory phenotype observed
152 through IHC and flow cytometry, reinforcing METTL5's regulatory role in tumor-
153 immune interactions.
154
155 **Loss of *Mettl5* enhances the response to immune checkpoint blockade**
156 Given that *Mettl5* knockout has been shown to enhance tumor-infiltrating capacity of
157 $CD8^+$ T cells, which play a critical role in antitumor immunity[56], we further asked
158 whether depleting *Mettl5* synergizes with immune checkpoint blockade. In C57BL/6N
159 mice bearing B16-F10 melanomas, *Mettl5*-KO tumors exhibited significantly reduced
160 growth compared to SCR controls following anti-PD-1 treatment (Fig. 3A).
161 Importantly, the combination of *Mettl5* depletion and anti-PD-1 therapy demonstrated
162 the most robust anti-tumor effect, with median survival prolonged by 3 days compared
163 to groups only administrated to anti-PD-1 antibody (Fig. 3A). Furthermore, this finding
164 was also recapitulated in the PD-1-resistant 4T1 breast cancer model. *Mettl5* loss
165 significantly boosted antitumor immune responses, including reduced tumor volumes,
166 and extended survival compared to other groups (Fig. 3B).
167
168 To further evaluate the synergic effect of *Mettl5* depletion and anti-PD-1 blockade, we
169 analyzed tumor-infiltrating immune cells in B16-F10 melanoma tissues using flow
170 cytometry. Compared to SCR tumors, *Mettl5*-KO tumors exhibited significantly higher
171 proportions of $CD8^+$ T, $CD4^+$ T cells, and NK cells among intratumor cells (Fig. 3C-D,
172 Fig. S3A-B). Previous studies indicated that anti-PD-1 therapy expanded tumor-
173 infiltrating cytotoxic immune cell populations, including $CD8^+$ T cells, and augmented
174 their functional activity (as measured by elevated CD107a expression)[57]. Notably,

175 *Mettl5*-KO synergized with anti-PD-1 treatment indeed enhanced these effects further
176 (Fig. 3D, S3B, rightmost panel). Together, our results revealed that *Mettl5* knockout
177 potently augments the anti-tumor efficacy of anti-PD-1 treatment, suggesting that
178 METTL5 inhibition can overcome immune checkpoint inhibitor resistance and improve
179 therapeutic outcomes in cancer immunotherapy.
180

181 ***Mettl5* depletion decreases ribosomal translation fidelity**

182 Recent advances have highlighted the critical role of RNA modifications in ribosome
183 function and translation regulation[58,59]. Though METTL5 had been identified as the
184 primary methyltransferase responsible for catalyzing m^6A1832 modification on 18S
185 rRNA[60-62], its precise molecular functions, particularly regarding its roles in translation
186 regulation under physiological and pathological conditions, remain poorly understood.
187 To uncover its functional roles, we first investigate the individual 3D environments of
188 m^6A1832 modification inside the ribosome. As shown in Fig. 4A-B, the m^6A1832 site
189 is located within the core region of the 40S subunit's decoding center, specifically at
190 the h44-h45 helical junction of 18S rRNA. Adjacent nucleotides, including A1831,
191 C1704, Cm1703, and G1702, stabilize the conformation of the modification site
192 through base stacking and hydrogen bonding (Fig. 4A). Additionally, these residues
193 directly interact with ribosomal proteins uS12, uS11, and uS5, which are known to play
194 pivotal roles in regulating the dynamics of the decoding center [63,64]. Specifically, uS12
195 and uS11 are involved in the precise recognition of mRNA codons by interacting with
196 the anticodon loop of tRNA[65-67]. These findings suggest that m^6A1832 methylation may
197 enhance the rigidity of h44 (a central helix in the decoding center) or optimize local
198 nucleotide-protein interactions, thereby reducing conformational fluctuations during
199 translation and improving ribosome proofreading capabilities to ensure translational
200 fidelity. Interestingly, the methylation enviroment of A1832-C1702 pair is conserved
201 from bacteria to mammal. In *E. coli*, although A1500 (corresponding A1832 in human)
202 is unmodified, its paired C1402 (C1702 in human) carries an m^4Cm modification (Fig.

203 4C), which is critical for maintaining the small ribosomal subunit rRNA structure, and
204 enhancing translation fidelity[68,69].
205
206 Based on the above structural and evolutionary evidences, we speculate that METTL5
207 is likely involved in controlling mRNA translation fidelity. To test this hypothesis, we
208 set up a dual-luciferase reporter system to assess the accuracy of mRNA translation
209 upon loss of *Mettl5* (Fig. 4D). In the control plasmids (without pre-stop/frameshift
210 mutations), no significant difference was observed in the Firefly/Renilla ratio between
211 SCR and KO cells, indicating that *Mettl5* knockout does not affect the basal translation
212 efficiency (Fig. 4E). However, the synthesis of mutant Firefly luciferase in *Mettl5*-KO
213 cells was significantly higher than that in SCR cells (Fig. 4E). Specifically, the UGA
214 stop codon group demonstrated increased ribosome readthrough of termination signals,
215 and the -1/+1 frameshift mutation groups revealed a reduced ability of ribosomes in
216 maintaining protein synthesis reading frame (Fig. 4E). These results directly support
217 the notion that *Mettl5* knockout decreases ribosomal translation fidelity, manifesting as
218 enhanced tolerance to termination signal readthrough and frameshift errors, thereby
219 promoting the expression of aberrant proteins encoded by mutant plasmids.
220
221 ***Mettl5* depletion induces immunogenic neoantigen production by promoting**
222 **cryptic translation**
223 Given the observed translational perturbations in *Mettl5*-KO cells, we hypothesized that
224 the impaired translational fidelity potentially induce the cryptic translation of Novel or
225 Unannotated Open Reading Frames (nuORFs). This could promote tumor neoantigen
226 generation and consequently enhance tumor immunogenicity[70,71]. To test this
227 hypothesis, we performed hierarchical prediction of translated nuORFs in *Mettl5*-KO
228 versus SCR tumor cells using ribosome profiling (Ribo-seq) (Fig. 4F, S4A, S4B). The
229 actively translated ORFs were categorized into annotated ORFs and nuORFs, and
230 nuORFs were further classified into shared nuORFs, KO-specific nuORFs (nuORFs

231 with TPM values 1.5-fold higher in the KO than SCR), and SCR-specific nuORFs.
232 Subsequently, all nuORFs were categorized into five subtypes based on previous
233 study[71]: novel ORFs, uORFs (upstream ORFs), dORFs (downstream ORFs),
234 overlap_uORFs (overlapping upstream ORFs), and overlap_dORFs (overlapping
235 downstream ORFs) (Fig. 4G). Further analysis revealed that nuORFs primarily
236 originate from untranslated regions of protein-coding genes, pseudogenes, and long
237 non-coding RNAs (lncRNAs) (Fig. S4C). In contrast to annotated ORFs, considerable
238 portion of nuORF translation initiation is heavily dependent on non-canonical start
239 codons (particularly CUG) (Fig. S4D), implying active translation in putative non-
240 coding genomic regions. Additionally, the polypeptides translated from nuORFs are
241 also significantly shorter than those produced by annotated ORFs (Fig. S4E).
242 Importantly, we found that though *Mettl5* knockout had minimal impact on translation
243 efficiency of annotated ORFs (Fig. S4F). Interestingly, *Mettl5* knockout significantly
244 enhanced the translation of novel nuORFs among the five subtypes of nuORFs (Fig.
245 4H). Moreover, further analysis of reading frame integrity revealed that in the annotated
246 ORF group, the SCR group had a higher in-frame rate than the KO group (Fig. S4G,
247 left), suggesting an increased probability of translation frameshifts of the annotated
248 ORFs in the KO group. As to the nuORF, the KO group exhibited a significantly higher
249 in-frame rate than the SCR group (Fig. S4G, right), indicating that the extent of
250 translation activities in non-coding regions are much higher in the KO than SCR group.
251
252 To verify whether the translated nuORFs have the potential to become neoantigens
253 presented by MHC-I, we confirmed the existence of nuORF-derived neoantigens
254 through MHC-I immunopeptidomics. Based on the property that neoantigens require a
255 polypeptide length of at least 8 amino acids, we selected nuORFs with amino acid
256 lengths no less than 8 as the reference database for the tandem mass spectral (MS/MS)
257 library search. Although the number of KO-specific nuORFs was less than that in the
258 SCR group, MS/MS search detected 16 neoantigens derived from nuORFs in KO group,

259 significantly higher than the number (only 3) of nuORF-derived neoantigens detected
260 in the SCR group (Fig. 4I, J). Together, these findings indicate that *Mettl5* loss enhances
261 production of neoantigens generated by mistranslation of nuORFs.
262
263 ***Mettl5* deficiency increases TCR clonal diversity in tumors**
264 Considering that *Mettl5*-deficient tumors increased neoantigen loads, we hypothesized
265 that *Mettl5* knockout would drive enhanced T-cell receptor (TCR) repertoire diversity
266 in tumor-bearing hosts. Therefore, we performed TCR sequencing on peripheral blood
267 samples from B16-F10 melanoma mouse models at experimental endpoints and
268 conducted comparative TCR repertoire analysis between *Mettl5*-KO and SCR groups.
269 The CDR3 length distribution histograms revealed conserved patterns between groups,
270 with dominant peaks observed at 10–15 amino acid (aa) lengths (Fig. S5A).
271 Quantitative analysis showed obvious differences in TCR repertoire diversity between
272 *Mettl5*-KO and SCR tumor-bearing mice (Fig. 5A). The Shannon entropy of the KO
273 group (mean = 11.5) was significantly higher than that of the SCR group (mean = 10.5,
274 $p < 0.05$), indicating greater TCR repertoire diversity in tumor-bearing hosts with
275 *Mettl5*-deficient tumors (Fig. 5A, left). Furthermore, the clonality index was
276 significantly lower in the KO group compared to the SCR group, suggesting reduced
277 dominance of private clones (Fig. 5A, right) and a more evenly distributed clonal
278 landscape in *Mettl5*-deficient tumor-bearing mice (Fig. 5B). Consistently, the diversity
279 estimations across Hill diversity profiles (Q values 0–6) demonstrated higher diversity
280 indices in the KO group (Fig. 5C). Therefore, the above results provided evidences that
281 *Mettl5*-deficient tumors enhance neoantigen-driven T-cell activation. This expanded
282 TCR landscape may improve recognition capacity for heterogeneous neoantigens
283 generated by aberrant translation, potentially strengthening anti-tumor immunity.
284
285 Based on our prior evidence that *Mettl5* deficiency enhances MHC-I-restricted
286 neoantigen presentation, we hypothesized that genetic ablation of β2-microglobulin

287 (*B2m*), a critical component of the MHC class I heterodimer, would abolish the
288 antitumor effects observed in METTL5 deficiency tumors. In order to test this
289 hypothesis, *B2m* gene was disrupted using the CRISPR-Cas9 and the knockout
290 efficiency was validated by Western blotting (Fig. S5B, S5C). In syngeneic tumor
291 models, we compared the growth kinetics of tumors derived from *Mettl5-B2m* double-
292 knockout cells and *B2m*-knockout scramble control cells. Both groups exhibited
293 comparable tumor growth rates throughout the experimental period, with no
294 statistically significant differences in tumor volume (Fig. 5D, left). In contrast, the
295 *Mettl5*-KO-only group recapitulated the tumor growth suppression previously observed,
296 confirming the specificity of the antitumor phenotype (Fig. 5D, left). Consistently, the
297 survival analysis also corroborated our hypothesis (Fig. 5D, right). These data
298 definitively established that MHC-I-dependent antigen presentation is indispensable for
299 the antitumor immunity elicited by *Mettl5* depletion.
300
301 Taken together, all these findings implicated that the rRNA modification mediated by
302 METTL5 likely plays a critical role in sustaining mRNA translation accuracy. In
303 murine tumor model, loss of *Mettl5* induces mistranslation and promotes the generation
304 of non-canonical translation-derived neoantigens, which in turn boost tumor immunity
305 and represent a novel strategy to enhance immunotherapy (Fig. 5E).
306

DISCUSSION

In current study, we identified METTL5 as a critical translation regulator in tumor immune evasion through integrated multi-omics analysis and functional validation. *Mettl5* depletion markedly enhances tumor neoantigen burden by activating translation of noncanonical open reading frame. This mechanism fundamentally differs from traditional mutation-derived neoantigens, as these nuORF-derived neoantigens don't rely on genomic mutation accumulation but dynamically expand antigenic diversity through disrupting translational fidelity, providing a novel strategy to overcome immunotherapy resistance.

Molecular mechanism of METTL5 regulating translation fidelity

The dual-luciferase reporter assays and Ribo-Seq analysis indicated that the mRNA translation fidelity is apparently dysregulated upon loss of *Mettl5*. At the molecular level, METTL5-mediated m^6A1832 modification resides at the h44-h45 helical junction of 18S rRNA, a critical site within the ribosomal decoding center responsible for maintaining codon-anticodon pairing accuracy[53,60,61]. Intriguingly, the m^6A or m^4C in the decoding center is dispensable for the ribosome biogensis and cellular viability[53,68], which implies that they may function primarily in fine-tuning ribosomal activity rather than being essential components. Our findings that METTL5-mediated m^6A modification ensures translation fidelity in mammals mirror the established role of m^4C1402 modification in the decoding center of *E. coli*[68,69], indicating a conserved mechanism for mRNA translation accuracy. However, how these modifications quantitatively affect ribosome function and translational fidelity of mRNA is still not fully understood for now. Future studies should focus on resolving dynamic conformational changes in the ribosomal decoding center following *METTL5* deletion through cryo-electron microscopy to elucidate atomic-level regulatory mechanisms.

Peptides derived from nuORFs mistranslation as novel sources of neoantigens

335 In terms of tumor immune microenvironment, *Mettl5*-depleted tumors exhibited a
336 pronounced "hot" phenotype. The flow cytometry analysis and single-cell sequencing
337 revealed increased $CD8^+$T cell infiltration density, elevated NK cell proportions, and a
338 T cell receptor (TCR) repertoire with a Shannon diversity index, which further validated
339 the concept that interventing mRNA translation is likely a novel strategy for generating
340 neoantigen and can be utilized for enhancing tumor immuotherapy. Compared to
341 genomic interventions, translational regulation offers unique advantages for neoantigen
342 development: First, the reversibility of translation allows dynamic control of ribosomal
343 function (e.g., modulating methylation levels at the decoding center here) to flexibly
344 adjust translational error rates, avoiding permanent genomic alterations caused by
345 CRISPR or DNA-damaging agents[70-76]. Second, as translational regulation does not
346 directly interfere with DNA sequences, its risks of carcinogenesis and off-target effects
347 are markedly reduced, enhancing clinical safety[70]. Critically, peptide variants generated
348 through translational misreading exhibit high spatiotemporal heterogeneity[73,75]. These
349 transiently existing non-self-epitopes can effectively evade immune editing pressures,
350 breaking immune tolerance induced by fixed mutation-derived epitopes[76]. which sheds
351 light on the future application of neoantigens derived from nuORF mistranslation.
352
353 **Targeting ribosome-related factors (RRFs) for enhancing tumor immunity**
354 Recent studies have explored diverse strategies to induce neoantigen generation by
355 targeting tRNA-related pathways, such as inhibiting tRNA modifiers or disrupting
356 tRNA aminoacetylation[76,77]. While these approaches have demonstrated promising
357 preclinical efficacy, their clinical applicability may be limited due to codon-specific
358 restrictions and low diversity of neoantigens produced. In contrast, ribosomal trans-
359 acting factors represent more versatile therapeutic targets. Besides METTL5 reported
360 in current work, multiple ribosome-related factors (RRFs) have been implicated in
361 tumor immunity. Notably, depletion of RPS28 had also been shown to enhance
362 immunogenicity[78]. These findings highlight the broader potential of ribosomal-targeted

interventions compared to tRNA-based strategies. On other hand, despite these therapeutic implications, clinical translation of RRFs-targeting strategies faces multiple challenges. The most critical concern is that reduced translational fidelity may lead to aberrant self-antigen production in healthy tissues, potentially triggering autoimmune reactions. Although RRFs are frequently overexpressed in tumors[79,80] long-term immunological monitoring remains necessary. Nevertheless, these findings highlight RRFs as promising therapeutic targets for cancer immunotherapy. Further investigation is warranted to explore pharmacological and genetic strategies targeting ribosome-related factors to modulate antigen presentation in cancer, particularly tumor immunity contexts.

In summary, our current study not only establishes ribosomal chemical modifications as critical mediators of tumor immune surveillance but also provides experimental evidence for "translational reprogramming" as a novel strategy to overcome current limitations in cancer immunotherapy.

379 **MATERIALS AND METHODS**

380 **Cell culture**

381 The B16-F10 melanoma cells and 4T1 breast cancer cells were purchased from Wuhan
382 Pricella Biotechnology. All cells were authenticated by STR profiling and testing for
383 mycoplasma contamination was performed with a MycAway one-step mycoplasma
384 detection kit (Yeasen, 40612ES25). All cells were cultured in Dulbecco's Modified
385 Eagle Medium (DMEM, Gibco) supplemented with 10% fetal bovine serum (FBS,
386 Biological Industries), 1% penicillin-streptomycin (Thermo Fisher Scientific), and 1%
387 SaveIt mycoplasma inhibitor (Hanbio Biotechnology). Cells were maintained in a
388 humidified incubator at 37°C with 5% CO_2 and routinely tested for bacterial and
389 mycoplasma contamination.

390

391 **Plasmid construction and Generation of knockout cell**

392 Knockout cells were generated using CRISPR/Cas9 technology. Two independent
393 sgRNAs (targeting *Mettl5* or *B2m* exon 2) were cloned into pL-CRISPR.EFS.GFP
394 plasmid separately. To generate *Mettl5* knockout cells, 2 μg of sgRNA vector that
395 targeting mouse *Mettl5* was transfected to the corresponding cells using Lipofectamine
396 3000 (Invitrogen). After 2 days' culture in DMEM medium, cells were screened
397 according to fluorescence and isolated into monoclons by flow cytometry. After 3
398 weeks' culture, colonies were screened out and confirmed by sequencing and RT-qPCR.
399 LCMS/MS was also used to further detected the changes of m^6A modification in SCR
400 and *Mettl5-KO* cells. To generate *Mettl5*-knockout plus *B2m* knockout B16-F10 cells,
401 2 μg of sgRNA vector that targeting mouse *B2m* was transfected to B16 SCR or *Mettl5-*
402 *KO* cells using Lipofectamine 3000 (Invitrogen). After 2 days' culture in DMEM
403 medium, cells were screened according to fluorescence and isolated into monoclons by
404 flow cytometry. After 3 weeks' culture, colonies were screened out and confirmed by
405 western blot.

406 sgRNA sequences targeting mouse *Mettl5* locus:

407 AGCATCGGAGCGGCAATGCTAGG

408 sgRNA sequences targeting mouse *B2m* locus:

409 AGTATACTCACGCCACCCACCGG

410

411 **Cell proliferation and colony formation**

412 For cell proliferation, B16-F10 (1.5×10^5 cells/well) and 4T1 (0.5×10^5 cells/well) cells
413 were seeded in a 24-well plate on day 0 and counted on day one until day 3 with a cell
414 counter (Thermo Fisher Scientific) to measure cell proliferation. For colony formation,
415 500 cells were seeded in a 6-well plate and cultured for six days. Cells were then fixed
416 with 4% formaldehyde (Beyotime) and stained with 0.1% crystal violet solution
417 (Solarbio). Next, the number and size of Cell colonies were measured.

418

419 **Western blot**

420 For western blotting, a six-well plate of cells at approximately 80-90% confluency was
421 lysed with 100 μL RIPA buffer on ice. Cell lysates were separated by 4-20% SDS-
422 PAGE, and the protein was then transferred to 0.4 μm polyvinylidene fluoride (PVDF,
423 Merck Millipore) membrane. After blocking with 5% milk in TBST, the membranes
424 were then incubated with the corresponding antibodies overnight at 4°C. Membranes
425 were incubated with secondary HRP-conjugated antibody (Proteintech) at room
426 temperature for 2 hours following three times washes with TBST and were washed
427 three times again before detected by the phosphoimager. The corresponding antibodies
428 included Monoclonal rabbit anti-B2m antibody with 1:5000 dilution (Abcam, ab75853)
429 and anti-GAPDH antibody with 1:5000 dilution (Proteintech, 10494-1-AP). Full and
430 uncropped Western blot images are shown in Fig. S6.

431

432 **Quantitative Reverse Transcription PCR (RT-qPCR)**

433 Total RNA was isolated from B16-F10 and 4T1 cells using Total RNA Isolation Kit
434 (Vazyme, RC112-01) and reverse-transcribed to cDNA by the use of RT reagent Kit

435 with gDNA Eraser (Takara, RR047A). Primers for quantitative RT-PCR (qPCR) were
436 designed using Primer-BLAST. Reactions were run on the real-time PCR machine
437 (QuantStudio 7 Flex) using TB Green PCR master- mix (Takara, RR430A). The
438 relative gene expression level was calculated with the comparative cycle threshold (CT)
439 method, and the relative number of target transcripts was normalized according to
440 mouse Gapdh gene. Data were plotted using GraphPad Prism 9
441 (https://www.graphpad.com). Each experiment was performed in triplicate. The
442 oligonucleotide primers used for PCR amplification are listed below:
443 Mettl5:
444 Forward primer: 5'- CTGAAGACTGCTTTGGGAATGGC-3';
445 Reserve primer: 5'- AATGCTGGTAGATCATATCGAAGC-3'.
446 Gapdh:
447 Forward primer: 5'-CATCACTGCCACCCAGAAGACTG-3';
448 Reserve primer: 5'- ATGCCAGTGAGCTTCCCGTTCAG-3'.
449
450 **Animal Sources**
451 Six- to 8-week-old female C57BL/6N mice were purchased from Beijing Vital River
452 Laboratory Animal Technology Co., Ltd. Six- to 8-week-old female Balb/c mice and
453 3- to 4-week-old female nude mice were obtained from GemPharmatech. All mice were
454 bred in a specific-pathogen-free (SPF) animal facility with a 12-h light/12-h dark cycle,
455 at 22.5 ± 1°C and 50 ± 5% relative humidity. All animal experiments were approved
456 by the Institutional Animal Care and Use Committee (IACUC) of Southern University
457 of Science and Technology.
458
459 ***In vivo* competition assay**
460 For generation of mCherry-labeled SCR and GFP-labeled *Mettl5* knockout KO cells,
461 lentiviral particles were produced by co-transfecting 293T cells with either the GFP or
462 mCherry plasmid along with the packaging plasmids pMD2.G and PsPAX2. B16 SCR

463 cells were transduced with the GFP-expressing lentivirus, while *Mettl5*-KO cells were
464 infected with the mCherry-expressing lentivirus. Following three days of culture, cells
465 were fluorescence-sorted by flow cytometry to isolate stable populations expressing the
466 respective markers. A 1:1 mixture of mCherry-labeled SCR cells and GFP-labeled KO
467 cells was prepared. This mixture was either subcutaneously injected into C57BL/6N
468 mice or co-cultured in vitro. Tumors were harvested 12 days post-injection, and the
469 relative proportions of GFP^+ (Mettl5-KO) and $mCherry^+$ (SCR) cells in both tumors
470 and in vitro cultures were quantified by BD Canto II flow cytometer (Flow Cytometry
471 Shared Facility, SUSTech University).
472
473 **Tumour growth in mice**
474 Syngeneic and xenogeneic subcutaneous tumor transplantation assays to evaluate
475 tumorigenicity of mettl5-deficient tumor cells. For syngeneic models, tumor cells were
476 resuspended in PBS (Gibco) and injected subcutaneously into the right dorsal flank of
477 C57BL/6N or Balb/c mice. For xenogeneic models, tumor cells were mixed with an
478 equal volume of Matrigel (Corning) at a 1:1 ratio before subcutaneous injection into
479 nude mice. Tumor volume was measured every other day starting from day 5 or 7 until
480 tumors reached a maximum size of 2000 mm^3, calculated as length × $width^2$. At the
481 experimental endpoint, tumors were harvested and weighed. Mouse survival curves
482 were plotted using endpoints: death or tumor volume exceeding 2000 mm^3.
483
484 **Preparation of tumor tissue single-cell suspension**
485 At the endpoint of the mouse tumor model, tumors were bluntly dissected intact using
486 surgical scissors and forceps (RWD). After all tumors were stripped, the mass of each
487 tumor sample was recorded and transferred to a 6-cm dish with appropriate HBSS
488 (Gibco). Using curved scissors (RWD), tumors were uniformly minced until passable
489 through a 1-mL pipette tip. Then, collagenase IV (0.5 mg/mL, Sigma) and DNase I
490 (100 U/mL) were added proportionally to the tumor volume. Digestion was performed

491 on a 37°C shaker at 80 rpm for 45 min. The tumor suspension was filtered through a
492 70-μm strainer, and single-cell suspension was obtained by centrifugation at 1500 rpm
493 for 10 min at 4°C, followed by three PBS washes. Finally, cells were collected, stained
494 with antibodies, and analyzed by flow cytometry.
495
496 **Analysis of tumour-infiltrating lymphocytes**
497 Single-cell suspensions of tumor tissues were prepared and incubated with 50 μL of a
498 solution containing anti-mouse CD16/32 (BioLegend, catalog #101320, diluted 1:50)
499 and anti-mouse Zombie NIR™ Fixable Viability Kit (APC-750, BioLegend, catalog
500 #423105, diluted 1:200) to block non-specific binding and label dead cells. After
501 incubation at 4°C for 10 minutes, a cocktail of surface antibodies for mouse immune
502 cell subset staining was prepared. Cells were stained with the antibody cocktail in 100
503 μL of tumor staining buffer (BioLegend, #420201) on ice at 4°C for 30 minutes. After
504 incubation, cells were washed twice with staining buffer and resuspended in 900 μL of
505 staining buffer. Counting beads (Invitroge) were added (100 μL per sample) to quantify
506 cell concentrations. Samples were analyzed using a BD Canto II flow cytometer (Flow
507 Cytometry Shared Facility, SUSTech University), with 300,000 $CD45^+$ events recorded
508 per sample. Data were analyzed using FlowJo (version 10).
509 The antibodies used were as follows: anti-mouse CD4 (Pacific Blue, BioLegend,
510 #100531, diluted 1:200); anti-mouse CD45 (Brilliant Violet 510, BioLegend, #103138,
511 diluted 1:100); anti-mouse CD19 (FITC, BioLegend, #115505, diluted 1:200); anti-
512 mouse CD8α (PerCP/Cyanine5.5, BioLegend, #100734, diluted 1:200); anti-mouse
513 NK-1.1 (PE, BioLegend, #108708, diluted 1:200);anti-mouse CD25 (PE/Dazzle 594,
514 BioLegend, #102048, diluted 1:200); anti-mouse TCR β chain (PE/Cyanine7,
515 BioLegend, #109222, diluted 1:200); anti-mouse CD107a (APC，BioLegend, #121615，
516 diluted 1:200); anti-mouse CD11c (APC/Fire™ 750, BioLegend, #117352, diluted
517 1:200).
518

519 **Immunohistochemistry (IHC) detection**

520 IHC was used to evaluate the expression of CD8α in tumor tissues and compare SCR
521 and Mettl5-KO samples. Paraffin-embedded tumor tissues were sectioned into 4-5 μm
522 thick slices and mounted on glass slides. The sections were deparaffinized using xylene
523 and alcohol, followed by antigen retrieval in a citrate buffer. Nonspecific binding was
524 blocked with an appropriate solution, and then a primary antibody specific to the CD8α
525 protein was applied and incubated overnight at 4°C. After washing, a secondary HRP-
526 conjugated antibody was added and incubated for one hour at room temperature. The
527 bound antibodies were visualized using an IHC detection substrate that produced a
528 colorimetric reaction. Counterstaining with hematoxylin was performed to highlight
529 cell nuclei. Images were captured using a microscope, and positive staining cells were
530 quantified within a defined area using image analysis software. Statistical analysis was
531 conducted to assess the differences in the number of stained cells between SCR and KO
532 samples, and the findings were reported with representative images, quantitative data,
533 and a discussion of the results.

534

535 **Luciferase Reporter Assay**

536 The dual luciferase reporter vector pmirGLO, which contains both firefly (F-Luc) and
537 Renilla (R-Luc) luciferases, was chosen for meauringing the changes of translational
538 activities. The original pmirGLO plasmids were engineered by introducing a UGA stop
539 codon or frameshift mutations (+1 or -1) into the firefly luciferase gene, respectively.
540 1 μg of wildtype or mutatant plasmids were transfected into B16-F10 WT or *Mettl5* KO
541 cells. After 48 hours of transfection, luciferase expression was measured using the
542 Dual-Glo Luciferase Assay System (Promega).

543

544 **Ribo-seq**

545 Two 15-cm plates of cells with approximately 80-90% confluency was used per group.
546 Cells were incubated with 100 μg/mL Cycloheximide (MCE) for 8 min at 37°C and

547 were then lysed on ice for 10min in 400uL lysis buffer (20 mM Tris–HCl pH 7.5, 150
548 mM NaCl, 5 mM $MgCl_2$, 1 mM DTT, 100 μg/mL Cycloheximide, 1% Triton X-100).
549 The supernatant was collected via centrifugation at 12 000 g for 10 min at 4 °C, and its'
550 absorbance at 260 nm was measured. The ribosomes with equal A260 in each group
551 were reserved for RNA sequencing. Added 15U RNase1 (Thermo Fisher Scientific) for
552 each 1OD of lysate, and incubated the reactions at 22°C for 40 min with gentle mixing.
553 Ribosome-protected fragments (RPFs) were collected by MicroSpin S-400 columns
554 (Cytiva) and purified by Zymo Research RNA Clean & Concentrator-25 kit (Zymo).
555 The RPFs were then separated with 15% polyacrylamide TBE–urea gel, excised the gel
556 slices between 17 and 34 nucleotides and recovered RNA from PAGE gel by ZR small-
557 RNA™ PAGE Recovery Kit (Zymo). Purified RNA was treated with PNK(NEB), and
558 the RNA library was prepared by VAHTSTM Small RNA Library Prep Kit for
559 Illumina®(Vazyme). The library concentration was analyzed using the VAHTSTM
560 Library Quantification Kit for Illumina®, and equimolar pools of libraries were
561 sequenced.
562
563 **MHC-Associated Peptide Enrichment for Immunopeptidomics Analysis**
564 For MHC-associated peptide isolation, we used two strategies: **1) MHC-I**
565 **immunoprecipitation (IP):** four 15-cm plates of B16 SCR or Mettl5-KO cells were
566 harvested and subsequently lysed on ice in 8 mL of 1× Lysis buffer (comprising 0.5%
567 NP-40, 50 mM Tris pH 8.0, 150 mM NaCl, and protease inhibitor) for 10 minutes.
568 Following lysis, protein extracts were obtained by centrifugation at 12,000 g for 10
569 minutes at 4°C. The supernatants were then incubated overnight with anti-mouse MHC-
570 I antibody conjugated to Pierce Protein A/G magnetic beads (Santa Cruz) to facilitate
571 immunoprecipitation. The bead-protein mixture was first treated with 1 mL of Wash
572 Buffer 1 (0.5% NP-40, 50 mM Tris-HCl pH 8.0, 150 mM NaCl, 5 mM EDTA, 100 μM
573 PMSF, and protease inhibitor) to remove nonspecifically bound proteins while
574 simultaneously inhibiting proteolytic degradation. Subsequent washes included 1 mL

575 of Wash Buffer 2 (50 mM Tris-HCl pH 8.0, 150 mM NaCl) to eliminate residual
576 detergent from the first step. High-affinity contaminants were then dissociated using 1
577 mL of Wash Buffer 3 (50 mM Tris-HCl pH 8.0, 450 mM NaCl), which applied high
578 ionic strength to disrupt non-specific interactions. Finally, a salt-free wash with 1 mL
579 of Wash Buffer 4 (50 mM Tris-HCl pH 8.0) ensured complete removal of residual salts,
580 thereby maintaining compatibility with downstream elution steps. Bound peptides were
581 released by treating the beads with 10% acetic acid (pH ~3.0), which denatures MHC
582 molecules and facilitates peptide dissociation. The eluate was then filtered through a 3
583 kDa molecular weight cut-off filter to remove the MHC-I α-chain, B2m protein, and
584 the corresponding MHC antibody. The eluted proteins were ultimately analyzed by
585 HPLC-MS to identify the MHC peptides. **2) Mild acid elution (MAE):** this was
586 performed on six 15 cm dishes of B16 control cells or *Mettl5*-KO cells stimulated with
587 100IU/mL IFN-γ for 24 h. Cells were treated on ice with pH 3.3 citric acid-phosphate
588 buffer for 5 min to dissociate MHC-antigen peptide complexes and release antigenic
589 peptides. After centrifugation at 10000 g, the supernatant was collected and filtered
590 through a 3 kDa molecular weight cutoff filter. The eluted proteins were analyzed by
591 HPLC-MS for MHC peptides.
592
593 **TCR library construction and T-Cell Receptor Repertoire Sequencing**
594 PBMCs were isolated from whole blood of C57BL/6N mice that had been inoculated
595 with either control B16-F10 cells or *Mettl5*-KO cells 12 days prior. DNA was extracted
596 from PBMC using a QIAamp DNA Blood Mini Kit (Qiagen), and the concentration
597 was tested using NanoDrop 2000 spectrophotometer (Thermo Fisher Scientific). The
598 DNA was used as a template for PCR amplification, which was performed to generate
599 the library of TCR. The step 1 PCR amplification protocol was as follows: 95 °C for 5
600 min; 95 °C for 30 s, 59 °C for 30 s; 72 °C for 1 min for 30 cycles; and 72 °C for 10 min.
601 The step 2 PCR amplification protocol was as follows: 98 °C for 2 min; 98 °C for 30 s,
602 65 °C for 30 s; 72 °C for 30 s for 10 cycles; and 72 °C for 5 min. The PCR products

603 were purified, and the barcodes were confirmed. The annealed region of these primers
604 was the CDR3 region, as shown by Multiplex PCR Amplifies. The CDR3 regions were
605 sequenced on Illumina NextSeq500 (MyGenostics). According to the sequencing depth,
606 the test covered about 90% of the TCR. The CDR3 regions were identified based on
607 the definition established by the International ImMunoGeneTics (IMGT)
608 (http://www.imgt.org/, accessed on 19 March 2021) collaboration, and the V, D, and J
609 segments contributing to each CDR3 region were identified by a standard algorithm.
610 Data were analysed using ImmunoSEQ Analyzer 3.0, an Adaptive Biotechnologies
611 online analysis platform.
612
613 **RNA-seq and Ribo-seq analysis**
614 Adapter sequences were removed from both Ribo-seq and RNA-seq reads using
615 TrimGalore (v0.6.7). For Ribo-seq data, reads shorter than 20 nucleotides or longer
616 than 35 nucleotides were discarded to ensure high-quality ribosome-protected fragment
617 selection. The trimmed reads were then aligned to rRNA and tRNA sequences using
618 Bowtie2 (v2.2.5)[81]. Reads that aligned to rRNA or tRNA were excluded, while the
619 remaining unaligned reads were retained for subsequent analysis. Processed reads were
620 aligned to the reference genome (gencode GRCh38) by the STAR (v2.7.10a)[82],
621 allowing for at most two mismatches. For Ribo-seq data, quality control and
622 translational profiles was analyzed by RiboseQC. Transcriptome assembly and
623 quantification were performed using StringTie (v2.1.7)[83]. Both read counts of Ribo-seq
624 and RNA-seq were converted to TPM (transcripts per million). Genes with sufficient
625 expression level (Ribo TPM > 1 and RNA TPM > 5) were subjected to further analysis.
626 Translation efficiency (TE) and the differentially-TE genes (DTEGS) were calculated
627 by RiboDiff (v0.2.2)[84]. GO term analysis were performed by Metascape
628 (https://metascape.org/gp/index.html). GraphPad Prismsoftware and R was used for
629 data presentation.
630

631 **Hierarchical prediction of translated ORFs across tissues**

632 In our study, we used the RiboCode[85] algorithm to detect actively translated open
633 reading frames (ORFs) with the parameters set as follows: a minimum fractional
634 threshold of ribosome profiling reads (-f0_percent 0.5), a primary start codon of ATG
635 (--start_codon ATG), alternative start codons of CTG, GTG, and TTG (--
636 alt_start_codons CTG, GTG, TTG), and a minimum amino acid length of 8 (--min-AA-
637 length 8). The identified ORFs were classified into several categories: "annotated"
638 ORFs, which overlap with annotated coding sequences (CDS) and share the same stop
639 codon; "uORFs", located upstream of the annotated CDS without overlap; "dORFs",
640 situated downstream of the annotated CDS without overlap; "Overlap_uORFs",
641 overlapping with the annotated CDS while being upstream; "Overlap_dORFs",
642 overlapping with the annotated CDS while being downstream; "Internal" ORFs, which
643 are internal to the annotated CDS but in a different reading frame; and "novel" ORFs,
644 originating from non-coding genes or non-coding transcripts of coding genes.
645 Additionally, we generated collapsed BED12 files for annotated ORFs
646 (annotatedORFdb.bed) and non-canonical ORFs (excluding the “annotated” type,
647 nuORFdb.bed), which served as references for subsequent analysis.

648

649 **Generating nuORFdb v.1.0**

650 The nuORFdb v.1.0 was constructed following the previous method [71]. Briefly, to count
651 the number of ribosomal profiling (RPF) reads aligned to ORFs, we first corrected the
652 read positions based on the offset distances between the 5' end of the reads and the
653 ribosomal A-sites. Subsequently, we employed the “rpfTPM” script from a prior study
654 (available at link) to quantify the number of in-frame reads. This script normalizes the
655 in-frame read counts to transcripts per million (TPM) against the nuORFdb.bed file.
656 ORFs with TPM values 1.5-fold higher in the KO samples compared to SCR samples
657 were designated as “KO-specific nuORFs”. Conversely, ORFs with TPM values 1.5-

658 fold higher in SCR samples relative to KO samples were classified as "SCR-specific
659 nuORFs".
660
661 **Estimation of absolute translation levels**
662 UniProt (reviewed mouse, release 2025_02) and the translated amino acid sequences
663 of larger nuORFs were used as reference databases for protein and peptide
664 identification. Notably, only those nuORFs longer than 8 aa were defined as potential
665 translated regions. The proteomics search was performed using SearchGUI (v4.2.17)
666 (https://github.com/compomics/searchgui) with MS-GF+ and Tide as search engines.
667 Carboxyamidomethylation of cysteine was set as a fixed modification, while oxidation
668 of methionine and proline were set as variable modifications. The enzyme specificity
669 was set to 'unspecific' and the precursor mass tolerance was set to 20 ppm
670 Hydrophobicity values for total PSM peptides were predicted with R package protViz
671 (v0.7.9) (https://github.com/cpanse/protViz).
672
673 **Statistical analysis**
674 No sample size calculations and blinding were performed. There was no method of
675 randomization. No samples or animals were excluded from analysis. Prism 9 software
676 (GraphPad) was used to analyze data from biological experiments by performing two-
677 tailed unpaired Student's t-tests. One-way analysis of variance (ANOVA) with Tukey's
678 test was used to compare multiple groups and two-way ANOVA was used to compare
679 cell proliferation analysis and tumor growth curves. P values $^{*}P<0.05$, $^{**}P<0.01$,
680 $^{***}P<0.001$, $^{****}P<0.0001$ were considered statistically significant.
681
682

ACKNOWLEDGEMENTS

We would like to thank all members in Hao Chen's Lab for their help and advice in experimental design. The authors would also like to acknowledge the technical support from Hua Li and Lin Lin at SUSTech CRF. This work was supported by Center for Computational Science and Engineering at Southern University of Science and Technology.

FUNDING

This work was supported by National Key Research and Development Program of China (2022YFC2702705), National Natural Science Foundation of China (32170604) and Pearl River Recruitment Program of Talents (2021QN02Y122) to H.C. This work was also supported by Shenzhen Key Laboratory of Gene Regulation and Systems Biology (Grant No. ZDSYS20200811144002008) from Shenzhen Innovation Committee of Science and Technology and Funding for Scientific Research and Innovation Team of The First Affiliated Hospital of Zhengzhou University (ZYCXTD2023004). This work was also supported by Shenzhen Science and Technology Fundamental Research Program grant RCYX20210706092045078 to W.L.

DECLARATION OF INTERESTS

The authors declare no competing interests.

AUTHOR CONTRIBUTIONS

H.C. and W.Q.L. designed and conceived the experiments. Y.Y.Z., X.Y.S., R.Q.W., F.L.L. and Y.L.C. performed experiments. Y.C.W. and X.Y.S. analyzed the data. Y.Y.Z., X.Y.S. and H.C. wrote the manuscript. All authors have read and approved the final manuscript.

DATA AND MATERIALS AVAILABILITY

The raw data of NGS is available in the GEO database under the accession number: GSE299761 (token: ozyvwyqmhnkdfcb). The mass spectrometry proteomics data have been deposited to the ProteomeXchange Consortium via the iProX partner repository with the dataset identifier PXD066586. The proteome datasets can be accessed at https://www.iprox.cn/page/PSV023.html;?url=1753447360479ycXH using password u9OM.

722 **REFERENCES**

723 1 Gajewski, T. F. *et al.* Immune resistance orchestrated by the tumor
724 microenvironment. *Immunol Rev* **213**, 131-145 (2006).
725 https://doi.org/10.1111/j.1600-065X.2006.00442.x
726 2 Joyce, J. A. & Fearon, D. T. T cell exclusion, immune privilege, and the tumor
727 microenvironment. *Science* **348**, 74-80 (2015).
728 https://doi.org/10.1126/science.aaa6204
729 3 Hegde, P. S. & Chen, D. S. Top 10 Challenges in Cancer Immunotherapy.
730 *Immunity* **52**, 17-35 (2020). https://doi.org/10.1016/j.immuni.2019.12.011
731 4 Sharma, P., Hu-Lieskovan, S., Wargo, J. A. & Ribas, A. Primary, Adaptive, and
732 Acquired Resistance to Cancer Immunotherapy. *Cell* **168**, 707-723 (2017).
733 https://doi.org/10.1016/j.cell.2017.01.017
734 5 Zaretsky, J. M. *et al.* Mutations Associated with Acquired Resistance to PD-1
735 Blockade in Melanoma. *N Engl J Med* **375**, 819-829 (2016).
736 https://doi.org/10.1056/NEJMoa1604958
737 6 McDonald, K. A. *et al.* Tumor Heterogeneity Correlates with Less Immune
738 Response and Worse Survival in Breast Cancer Patients. *Ann Surg Oncol* **26**,
739 2191-2199 (2019). https://doi.org/10.1245/s10434-019-07338-3
740 7 El-Sayes, N., Vito, A. & Mossman, K. Tumor Heterogeneity: A Great Barrier in
741 the Age of Cancer Immunotherapy. *Cancers (Basel)* **13** (2021).
742 https://doi.org/10.3390/cancers13040806
743 8 Weiskopf, K. *et al.* Engineered SIRPalpha variants as immunotherapeutic
744 adjuvants to anticancer antibodies. *Science* **341**, 88-91 (2013).
745 https://doi.org/10.1126/science.1238856
746 9 Chabner, B. A. & Roberts, T. G., Jr. Timeline: Chemotherapy and the war on
747 cancer. *Nat Rev Cancer* **5**, 65-72 (2005). https://doi.org/10.1038/nrc1529
748 10 Ahmed, M. M. *et al.* Harnessing the potential of radiation-induced immune
749 modulation for cancer therapy. *Cancer Immunol Res* **1**, 280-284 (2013).
750 https://doi.org/10.1158/2326-6066.CIR-13-0141
751 11 Pao, W. *et al.* Acquired resistance of lung adenocarcinomas to gefitinib or
752 erlotinib is associated with a second mutation in the EGFR kinase domain. *PLoS*
753 *Med* **2**, e73 (2005). https://doi.org/10.1371/journal.pmed.0020073
754 12 Oh, T. K. *et al.* Long-Term Oncologic Outcomes, Opioid Use, and
755 Complications after Esophageal Cancer Surgery. *J Clin Med* **7** (2018).
756 https://doi.org/10.3390/jcm7020033
757 13 Nelson, D. B. *et al.* Surgical margins and risk of local recurrence after wedge
758 resection of colorectal pulmonary metastases. *J Thorac Cardiovasc Surg* **157**,
759 1648-1655 (2019). https://doi.org/10.1016/j.jtcvs.2018.10.156
760 14 Sakuishi, K. *et al.* Targeting Tim-3 and PD-1 pathways to reverse T cell
761 exhaustion and restore anti-tumor immunity. *J Exp Med* **207**, 2187-2194 (2010).
762 https://doi.org/10.1084/jem.20100643
763 15 Sharma, P. & Allison, J. P. The future of immune checkpoint therapy. *Science*

764 **348**, 56-61 (2015). https://doi.org/10.1126/science.aaa8172
765 16 Topalian, S. L., Taube, J. M., Anders, R. A. & Pardoll, D. M. Mechanism-driven
766 biomarkers to guide immune checkpoint blockade in cancer therapy. *Nat Rev*
767 *Cancer* **16**, 275-287 (2016). https://doi.org/10.1038/nrc.2016.36
768 17 Puig-Saus, C. *et al.* Neoantigen-targeted CD8(+) T cell responses with PD-1
769 blockade therapy. *Nature* **615**, 697-704 (2023). https://doi.org/10.1038/s41586-
770 023-05787-1
771 18 Carreno, B. M. *et al.* Cancer immunotherapy. A dendritic cell vaccine increases
772 the breadth and diversity of melanoma neoantigen-specific T cells. *Science* **348**,
773 803-808 (2015). https://doi.org/10.1126/science.aaa3828
774 19 Borgers, J. S. W. *et al.* Personalized, autologous neoantigen-specific T cell
775 therapy in metastatic melanoma: a phase 1 trial. *Nat Med* **31**, 881-893 (2025).
776 https://doi.org/10.1038/s41591-024-03418-4
777 20 Braun, D. A. *et al.* A neoantigen vaccine generates antitumour immunity in renal
778 cell carcinoma. *Nature* **639**, 474-482 (2025). https://doi.org/10.1038/s41586-
779 024-08507-5
780 21 Danelli, L. Personalized neoantigen therapy for melanoma immunotherapy. *Nat*
781 *Cancer* **5**, 1783 (2024). https://doi.org/10.1038/s43018-024-00850-w
782 22 Ott, P. A. *et al.* An immunogenic personal neoantigen vaccine for patients with
783 melanoma. *Nature* **547**, 217-221 (2017). https://doi.org/10.1038/nature22991
784 23 Ott, P. A. *et al.* A Phase Ib Trial of Personalized Neoantigen Therapy Plus Anti-
785 PD-1 in Patients with Advanced Melanoma, Non-small Cell Lung Cancer, or
786 Bladder Cancer. *Cell* **183**, 347-362 e324 (2020).
787 https://doi.org/10.1016/j.cell.2020.08.053
788 24 Parkhurst, M. *et al.* Adoptive transfer of personalized neoantigen-reactive TCR-
789 transduced T cells in metastatic colorectal cancer: phase 2 trial interim results.
790 *Nat Med* **30**, 2586-2595 (2024). https://doi.org/10.1038/s41591-024-03109-0
791 25 Wang, M. *et al.* Humanized dual-targeting antibody-drug conjugates specific to
792 MET and RON receptors as a pharmaceutical strategy for the treatment of
793 cancers exhibiting phenotypic heterogeneity. *Acta Pharmacol Sin* (2025).
794 https://doi.org/10.1038/s41401-024-01458-7
795 26 Lim, Z. F. & Ma, P. C. Emerging insights of tumor heterogeneity and drug
796 resistance mechanisms in lung cancer targeted therapy. *J Hematol Oncol* **12**,
797 134 (2019). https://doi.org/10.1186/s13045-019-0818-2
798 27 Dash, P. *et al.* Quantifiable predictive features define epitope-specific T cell
799 receptor repertoires. *Nature* **547**, 89-93 (2017).
800 https://doi.org/10.1038/nature22383
801 28 Tran, E. *et al.* Immunogenicity of somatic mutations in human gastrointestinal
802 cancers. *Science* **350**, 1387-1390 (2015).
803 https://doi.org/10.1126/science.aad1253
804 29 Tran, E. *et al.* Cancer immunotherapy based on mutation-specific CD4+ T cells
805 in a patient with epithelial cancer. *Science* **344**, 641-645 (2014).

https://doi.org/10.1126/science.1251102

30 Lu, Y. C. *et al.* Mutated PPP1R3B is recognized by T cells used to treat a melanoma patient who experienced a durable complete tumor regression. *J Immunol* **190**, 6034-6042 (2013). https://doi.org/10.4049/jimmunol.1202830

31 Alban, T. J. *et al.* Neoantigen immunogenicity landscapes and evolution of tumor ecosystems during immunotherapy with nivolumab. *Nat Med* **30**, 3209-3222 (2024). https://doi.org/10.1038/s41591-024-03240-y

32 Lopez, J. *et al.* Autogene cevumeran with or without atezolizumab in advanced solid tumors: a phase 1 trial. *Nat Med* **31**, 152-164 (2025). https://doi.org/10.1038/s41591-024-03334-7

33 Huber, F. *et al.* A comprehensive proteogenomic pipeline for neoantigen discovery to advance personalized cancer immunotherapy. *Nat Biotechnol* (2024). https://doi.org/10.1038/s41587-024-02420-y

34 Liu, C. *et al.* KRAS-G12D mutation drives immune suppression and the primary resistance of anti-PD-1/PD-L1 immunotherapy in non-small cell lung cancer. *Cancer Commun (Lond)* **42**, 828-847 (2022). https://doi.org/10.1002/cac2.12327

35 Platten, M. *et al.* A vaccine targeting mutant IDH1 in newly diagnosed glioma. *Nature* **592**, 463-468 (2021). https://doi.org/10.1038/s41586-021-03363-z

36 Schumacher, T. *et al.* A vaccine targeting mutant IDH1 induces antitumour immunity. *Nature* **512**, 324-327 (2014). https://doi.org/10.1038/nature13387

37 Hsiue, E. H. *et al.* Targeting a neoantigen derived from a common TP53 mutation. *Science* **371** (2021). https://doi.org/10.1126/science.abc8697

38 Rojas, L. A. *et al.* Personalized RNA neoantigen vaccines stimulate T cells in pancreatic cancer. *Nature* **618**, 144-150 (2023). https://doi.org/10.1038/s41586-023-06063-y

39 Keskin, D. B. *et al.* Neoantigen vaccine generates intratumoral T cell responses in phase Ib glioblastoma trial. *Nature* **565**, 234-239 (2019). https://doi.org/10.1038/s41586-018-0792-9

40 Hu, Z. *et al.* Personal neoantigen vaccines induce persistent memory T cell responses and epitope spreading in patients with melanoma. *Nat Med* **27**, 515-525 (2021). https://doi.org/10.1038/s41591-020-01206-4

41 Apoorvi, T., Yury, P., Iryna, V. & Michelle, K. Phosphopeptide Neoantigens as Emerging Targets in Cancer Immunotherapy. *J Cancer Immunol (Wilmington)* **6**, 135-147 (2024). https://doi.org/10.33696/cancerimmunol.6.094

42 Gubin, M. M. *et al.* Checkpoint blockade cancer immunotherapy targets tumour-specific mutant antigens. *Nature* **515**, 577-581 (2014). https://doi.org/10.1038/nature13988

43 McGranahan, N. *et al.* Clonal neoantigens elicit T cell immunoreactivity and sensitivity to immune checkpoint blockade. *Science* **351**, 1463-1469 (2016). https://doi.org/10.1126/science.aaf1490

44 Schumacher, T. N. & Schreiber, R. D. Neoantigens in cancer immunotherapy.

Science **348**, 69-74 (2015). https://doi.org/10.1126/science.aaa4971

45 Yadav, M. *et al.* Predicting immunogenic tumour mutations by combining mass spectrometry and exome sequencing. *Nature* **515**, 572-576 (2014). https://doi.org/10.1038/nature14001

46 Rosenberg, S. A. & Restifo, N. P. Adoptive cell transfer as personalized immunotherapy for human cancer. *Science* **348**, 62-68 (2015). https://doi.org/10.1126/science.aaa4967

47 Snyder, A. *et al.* Genetic basis for clinical response to CTLA-4 blockade in melanoma. *N Engl J Med* **371**, 2189-2199 (2014). https://doi.org/10.1056/NEJMoa1406498

48 Jackson, S. P. & Bartek, J. The DNA-damage response in human biology and disease. *Nature* **461**, 1071-1078 (2009). https://doi.org/10.1038/nature08467

49 Brown, J. S., O'Carrigan, B., Jackson, S. P. & Yap, T. A. Targeting DNA Repair in Cancer: Beyond PARP Inhibitors. *Cancer Discov* **7**, 20-37 (2017). https://doi.org/10.1158/2159-8290.CD-16-0860

50 Olive, J. F. *et al.* Accounting for tumor heterogeneity when using CRISPR-Cas9 for cancer progression and drug sensitivity studies. *PLoS One* **13**, e0198790 (2018). https://doi.org/10.1371/journal.pone.0198790

51 Parsels, L. A. *et al.* Translation of DNA Damage Response Inhibitors as Chemoradiation Sensitizers From the Laboratory to the Clinic. *Int J Radiat Oncol Biol Phys* **111**, e38-e53 (2021). https://doi.org/10.1016/j.ijrobp.2021.07.1708

52 Kovacs, S. A., Fekete, J. T. & Gyorffy, B. Predictive biomarkers of immunotherapy response with pharmacological applications in solid tumors. *Acta Pharmacol Sin* **44**, 1879-1889 (2023). https://doi.org/10.1038/s41401-023-01079-6

53 van Tran, N. *et al.* The human 18S rRNA m6A methyltransferase METTL5 is stabilized by TRMT112. *Nucleic Acids Res* **47**, 7719-7733 (2019). https://doi.org/10.1093/nar/gkz619

54 Chen, H. *et al.* METTL5, an 18S rRNA-specific m^6A methyltransferase, modulates expression of stress response genes. *bioRxiv*, 2020.2004.2027.064162 (2020). https://doi.org/10.1101/2020.04.27.064162

55 Sepich-Poore, C. *et al.* The METTL5-TRMT112 N^6-methyladenosine methyltransferase complex regulates mRNA translation via 18S rRNA methylation. *Journal of Biological Chemistry* **298** (2022). https://doi.org/10.1016/j.jbc.2022.101590

56 Golstein, P. & Griffiths, G. M. An early history of T cell-mediated cytotoxicity. *Nat Rev Immunol* **18**, 527-535 (2018). https://doi.org/10.1038/s41577-018-0009-3

57 Aktas, E., Kucuksezer, U. C., Bilgic, S., Erten, G. & Deniz, G. Relationship between CD107a expression and cytotoxic activity. *Cell Immunol* **254**, 149-154 (2009). https://doi.org/10.1016/j.cellimm.2008.08.007

58 Delaunay, S., Helm, M. & Frye, M. RNA modifications in physiology and disease: towards clinical applications. *Nat Rev Genet* **25**, 104-122 (2024). https://doi.org/10.1038/s41576-023-00645-2

59 Milenkovic, I. & Novoa, E. M. Dynamic rRNA modifications as a source of ribosome heterogeneity. *Trends Cell Biol* **35**, 604-614 (2025). https://doi.org/10.1016/j.tcb.2024.10.001

60 Xing, M. *et al.* The 18S rRNA m(6) A methyltransferase METTL5 promotes mouse embryonic stem cell differentiation. *EMBO Rep* **21**, e49863 (2020). https://doi.org/10.15252/embr.201949863

61 Rong, B. *et al.* Ribosome 18S m(6)A Methyltransferase METTL5 Promotes Translation Initiation and Breast Cancer Cell Growth. *Cell Rep* **33**, 108544 (2020). https://doi.org/10.1016/j.celrep.2020.108544

62 Li, X., Yang, G., Ma, L., Tang, B. & Tao, T. N(6)-methyladenosine (m(6)A) writer METTL5 represses the ferroptosis and antitumor immunity of gastric cancer. *Cell Death Discov* **10**, 402 (2024). https://doi.org/10.1038/s41420-024-02166-1

63 Khatter, H., Myasnikov, A. G., Natchiar, S. K. & Klaholz, B. P. Structure of the human 80S ribosome. *Nature* **520**, 640-645 (2015). https://doi.org/10.1038/nature14427

64 Zhu, X., Cruz, V. E., Zhang, H., Erzberger, J. P. & Mendell, J. T. Specific tRNAs promote mRNA decay by recruiting the CCR4-NOT complex to translating ribosomes. *Science* **386**, eadq8587 (2024). https://doi.org/10.1126/science.adq8587

65 Milicevic, N., Jenner, L., Myasnikov, A., Yusupov, M. & Yusupova, G. mRNA reading frame maintenance during eukaryotic ribosome translocation. *Nature* **625**, 393-400 (2024). https://doi.org/10.1038/s41586-023-06780-4

66 Djumagulov, M. *et al.* Accuracy mechanism of eukaryotic ribosome translocation. *Nature* **600**, 543-546 (2021). https://doi.org/10.1038/s41586-021-04131-9

67 Holm, M. *et al.* mRNA decoding in human is kinetically and structurally distinct from bacteria. *Nature* **617**, 200-207 (2023). https://doi.org/10.1038/s41586-023-05908-w

68 Kimura, S. & Suzuki, T. Fine-tuning of the ribosomal decoding center by conserved methyl-modifications in the Escherichia coli 16S rRNA. *Nucleic Acids Res* **38**, 1341-1352 (2010). https://doi.org/10.1093/nar/gkp1073

69 Baudin-Baillieu, A. *et al.* Nucleotide modifications in three functionally important regions of the Saccharomyces cerevisiae ribosome affect translation accuracy. *Nucleic Acids Res* **37**, 7665-7677 (2009). https://doi.org/10.1093/nar/gkp816

70 Laumont, C. M. *et al.* Noncoding regions are the main source of targetable tumor-specific antigens. *Sci Transl Med* **10** (2018). https://doi.org/10.1126/scitranslmed.aau5516

71 Ouspenskaia, T. *et al.* Unannotated proteins expand the MHC-I-restricted immunopeptidome in cancer. *Nat Biotechnol* **40**, 209-217 (2022). https://doi.org/10.1038/s41587-021-01021-3

72 Laumont, C. M. *et al.* Global proteogenomic analysis of human MHC class I-associated peptides derived from non-canonical reading frames. *Nat Commun* **7**, 10238 (2016). https://doi.org/10.1038/ncomms10238

73 Mohler, K. & Ibba, M. Translational fidelity and mistranslation in the cellular response to stress. *Nat Microbiol* **2**, 17117 (2017). https://doi.org/10.1038/nmicrobiol.2017.117

74 Chong, C. *et al.* Integrated proteogenomic deep sequencing and analytics accurately identify non-canonical peptides in tumor immunopeptidomes. *Nat Commun* **11**, 1293 (2020). https://doi.org/10.1038/s41467-020-14968-9

75 Ruiz Cuevas, M. V. *et al.* Most non-canonical proteins uniquely populate the proteome or immunopeptidome. *Cell Rep* **34**, 108815 (2021). https://doi.org/10.1016/j.celrep.2021.108815

76 Weller, C. *et al.* Translation dysregulation in cancer as a source for targetable antigens. *Cancer Cell* **43**, 823-840 e818 (2025). https://doi.org/10.1016/j.ccell.2025.03.003

77 Pataskar, A. *et al.* Tryptophan depletion results in tryptophan-to-phenylalanine substitutants. *Nature* **603**, 721-727 (2022). https://doi.org/10.1038/s41586-022-04499-2

78 Wei, J. *et al.* Ribosomal Proteins Regulate MHC Class I Peptide Generation for Immunosurveillance. *Mol Cell* **73**, 1162-1173 e1165 (2019). https://doi.org/10.1016/j.molcel.2018.12.020

79 Ramalho, S., Dopler, A. & Faller, W. J. Ribosome specialization in cancer: a spotlight on ribosomal proteins. *NAR Cancer* **6**, zcae029 (2024). https://doi.org/10.1093/narcan/zcae029

80 Truitt, M. L. & Ruggero, D. New frontiers in translational control of the cancer genome. *Nat Rev Cancer* **16**, 288-304 (2016). https://doi.org/10.1038/nrc.2016.27

81 Langmead, B., Trapnell, C., Pop, M. & Salzberg, S. L. Ultrafast and memory-efficient alignment of short DNA sequences to the human genome. *Genome Biol* **10**, R25 (2009). https://doi.org/10.1186/gb-2009-10-3-r25

82 Dobin, A. *et al.* STAR: ultrafast universal RNA-seq aligner. *Bioinformatics* **29**, 15-21 (2013). https://doi.org/10.1093/bioinformatics/bts635

83 Pertea, M. *et al.* StringTie enables improved reconstruction of a transcriptome from RNA-seq reads. *Nat Biotechnol* **33**, 290-295 (2015). https://doi.org/10.1038/nbt.3122

84 Zhong, Y. *et al.* RiboDiff: detecting changes of mRNA translation efficiency from ribosome footprints. *Bioinformatics* **33**, 139-141 (2017). https://doi.org/10.1093/bioinformatics/btw585

85 Xiao, Z. *et al.* De novo annotation and characterization of the translatome with

ribosome profiling data. *Nucleic Acids Res* **46**, e61 (2018). https://doi.org/10.1093/nar/gky179

978 **FIGURE LEGENDS**

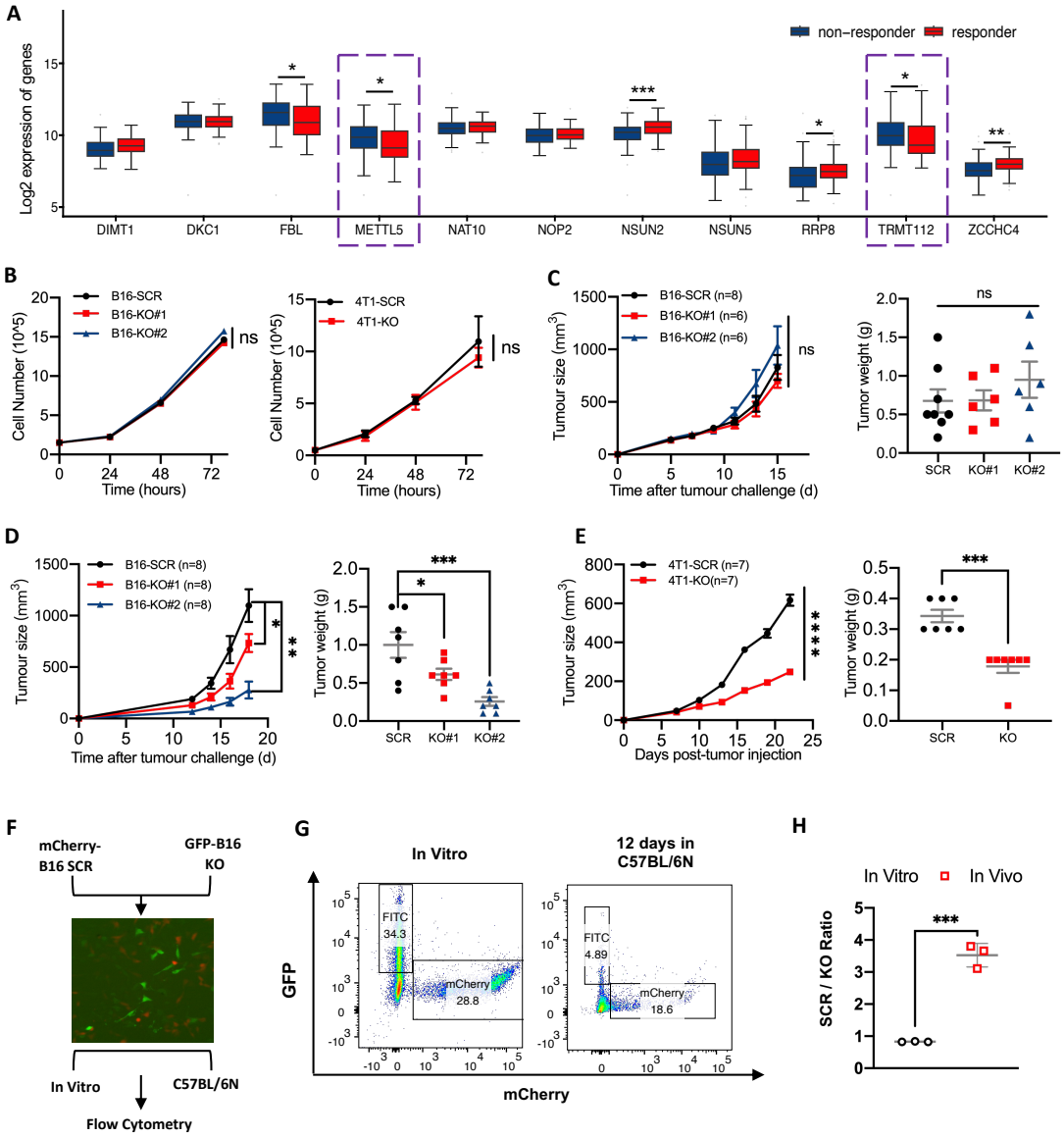

979

980 **Fig. 1: *METTL5* depletion attenuates tumour growth**

981 **A**, Relationship between the expression levels of ribosomal RNA modifiers and
982 response to immune checkpoint blockade (ICB) therapy. METTL5 and TRMT112 are
983 highlighted with purple dashed boxes.

984 **B**, *In vitro* cell growth assay of SCR and *Mettl5*-KO cells in B16-F10 (left) and 4T1
985 (right) cell lines.

986 **C**, Growth curve of tumors in nude mice subcutaneously implanted with B16-F10 SCR
987 or *Mettl5* deficiency cells. The tumor growth (left) and final tumor weights (right) were
988 compared.

D, Growth curve of tumors in C57BL/6N immunocompetent mice subcutaneously implanted with B16-F10 SCR or *Mettl5*-KO cells. The tumor growth (left) and final tumor weights (right) were compared.

E, Growth curve of tumors in Balb/c immunocompetent mice subcutaneously implanted with 4T1 SCR or *Mettl5*-KO cells. The tumor growth (left) and final tumor weights (right) were compared.

F-H, *In vivo* competition assay between mCherry-labeled SCR control and GFP-labeled *Mettl5*-KO B16-F10 cells. Schematic diagram of the competitive growth assay (**F**). mCherry-labeled SCR and GFP-labeled-KO cells were mixed at a 1:1 ratio and either subcutaneously injected into C57BL/6N mice or co-cultured *in vitro*. Cell ratios were quantified by flow cytometry on Day 12. Representative flow cytometry plots showing the composition of SCR and *Mettl5*-KO cells (**G**). Quantitative analysis of cell population ratios (**H**).

Note: A, Data retrieved from NCBI Gene Expression Omnibus (GEO) were presented as median (IQR 25-75%, n=154). Student's t-tests. **B**, two-way ANOVA. **C**, **D**, two-way ANOVA (left) and One-way ANOVA with Tukey's test (right). **E**, two-way ANOVA (left) and Student's t-tests (right). **H**, Student's t-tests. **B**, **H**, Data were represented as mean ± SD (n=3). **C**, **D**, **E**, Data were presented as mean ± SEM. **P*<0.05, ***P*<0.01, ****P*<0.001, ns: not significant.

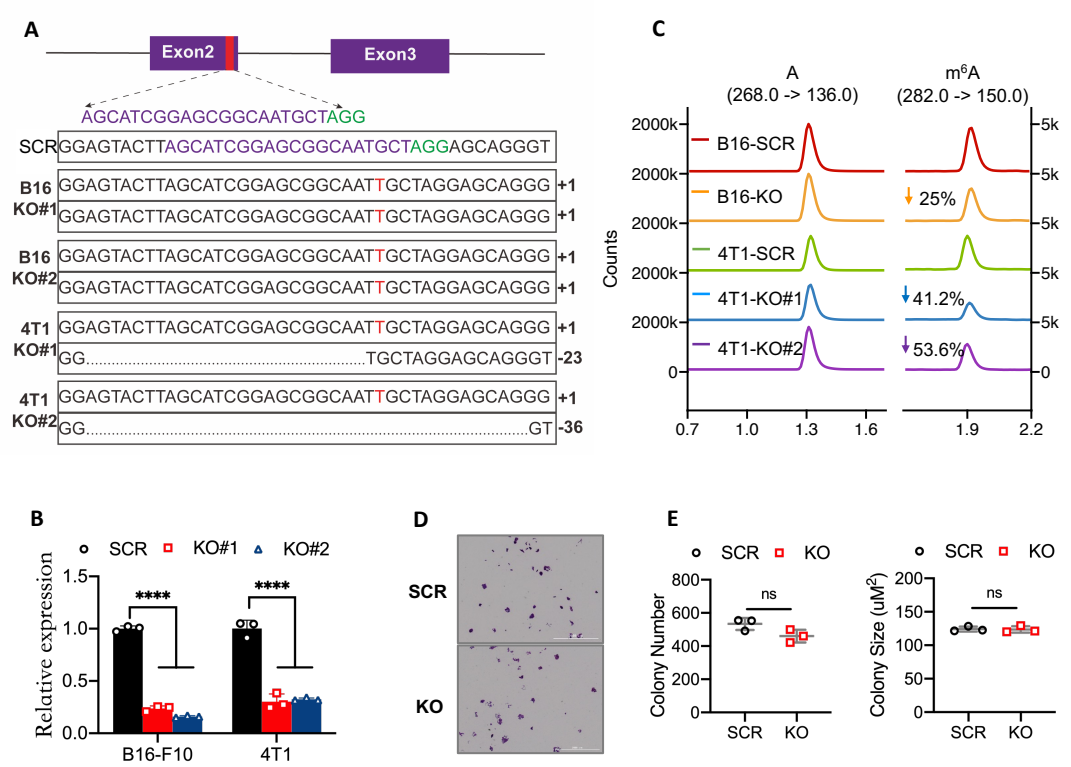

Fig. S1: Genetic ablation of *Mettl5* via CRISPR-Cas9 and its effect on tumour-cell growth *in vitro*

A, Schematic diagram of sgRNA targeting mouse *Mettl5* locus. Sanger sequencing was used to confirm CRISPR-Cas9-mediated knockout.

B, Knockout of *Mettl5* in B16-F10 cells and 4T1 cells were verified by Real-time quantitative PCR analysis.

C, HPLC-MS/MS analysis of m^6A/A levels in total RNA purified from the SCR and *Mettl5* KO cells.

D, **E**, Colony-formation assay of WT and *Mettl5* KO B16-F10 cells. 500 cells were seeded in a 6-well plate and cultured for six days, representative pictures (**D**) were taken, and the colony numbers and sizes (**E**) were measured.

Note: B, One-way ANOVA with Tukey's test. **E**, Student's t-tests (right). **B**, **E**, Data were represented as mean ± SD (n=3). ****P<0.0001, ns: not significant.

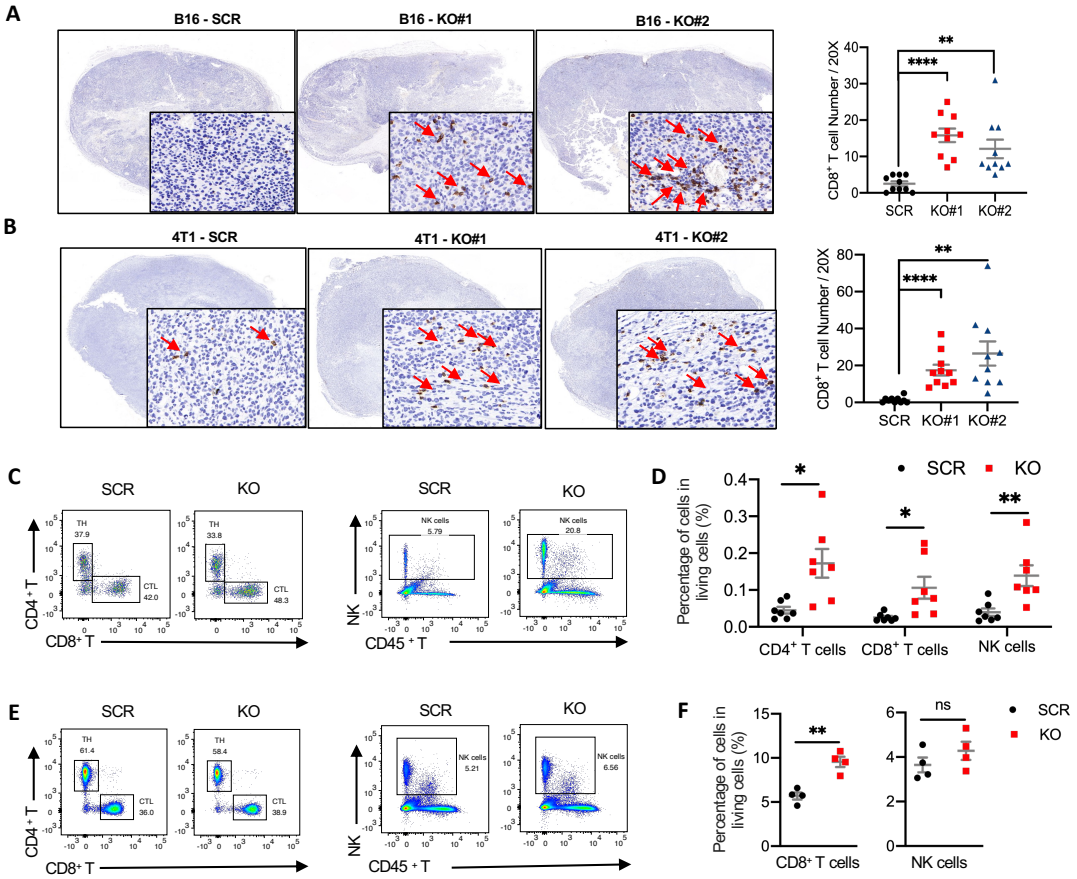

Fig. 2: *Mettl5* deficiency enhances tumor immune cell infiltration

A, **B**, Immunohistochemistry (IHC) detected $CD8^+$ cells in *Mettl5*-KO tumor tissues derived from B16-F10 (**A**) and 4T1 (**B**) models. Representative images (left) and quantified $CD8^+$ cell counts (right) are shown. 10 random 20× fields per sample were analyzed. $CD8^+$ cells are indicated by red arrows.

C-F, Flow cytometry analysis of immune cell populations in the tumor microenvironment (**C**) and spleen (**E**) of C57BL/6N mice inoculated with SCR or *Mettl5*-KO B16-F10 cells, and representative flow cytometry image showing the distribution of $CD4^+$ T cells, $CD8^+$ T cells (left) and NK cells(right). The relative frequency of immune cells amongst living cells from tumors (**D**) and spleen (**F**) were assessed.

Note: A, **B**, One-way ANOVA with Tukey's test. **D**, **F**, Student's t-tests. **A**, **B**, **D**, **F**, Data were represented as mean ± SD. **P*<0.05, ***P*<0.01, *****P*<0.0001, ns: not significant.

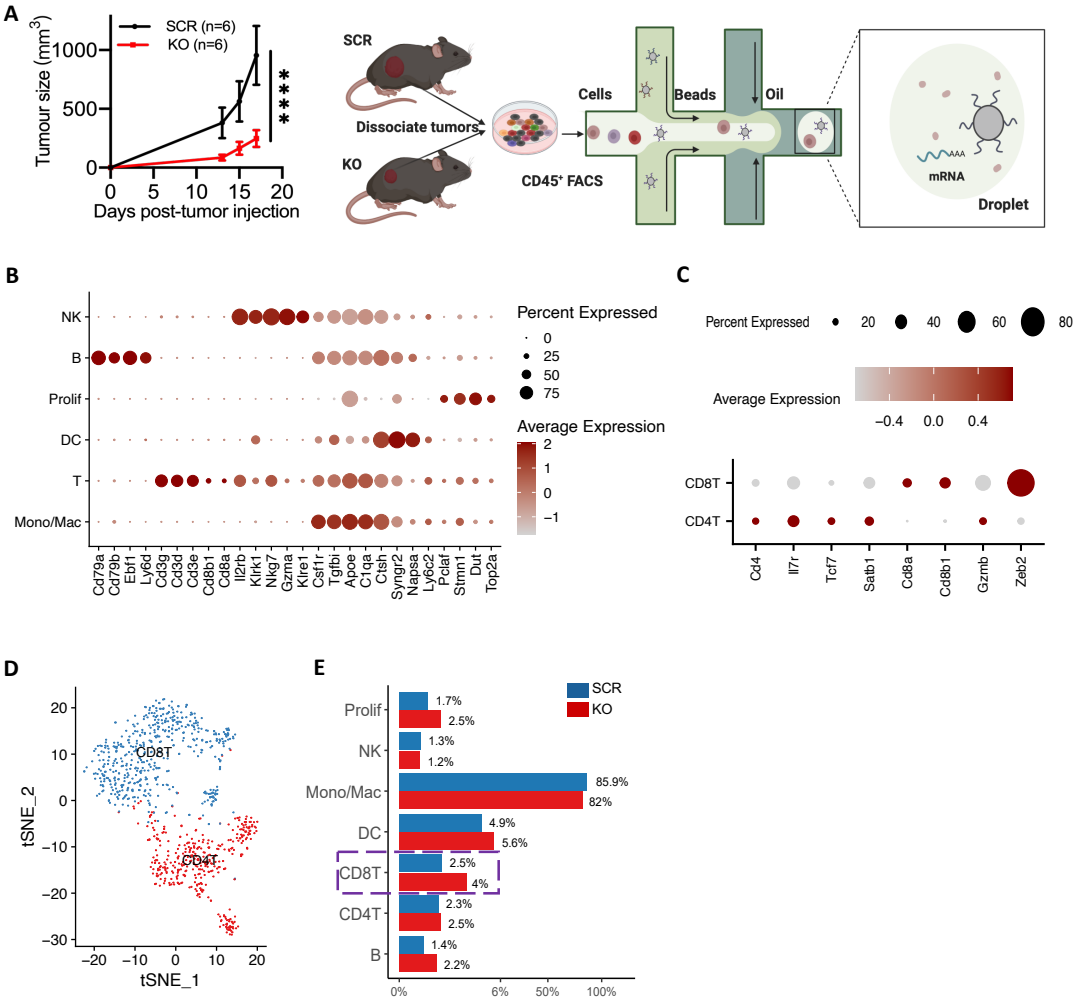

Fig. S2: Analysis of the tumor immune cell infiltration by scRNA-seq

A, Workflow schematic of single-cell sequencing for tumor tissues. In vivo tumor growth kinetics in C57BL/6 mice inoculated with SCR or *Mettl5*-KO B16-F10 cells. Tumors were excised and dissociated at day 18 post-inoculation, followed by $CD45^+$ immune cell enrichment and single-cell sequencing.

B, C, Dot plot illustrates the clustering analysis results of single-cell sequencing data (**B**). T cells were isolated from the total immune cell population and further stratified into $CD8^+$ T cells and $CD4^+$ T cell subsets (**C**). Dot color indicates expression level and dot size indicates the proportion of each cell type expressing each gene.

D, t-SNE plots show T-cell subpopulations derived from tumors, including $CD4^+$ T-cell and $CD8^+$ T-cell subpopulations.

1051 **E**, Bar chart shows the proportion of tumor-infiltrating immune cell populations, with

1052 blue representing the *Mettl5*- knockout group and red the control group.

1053

1054

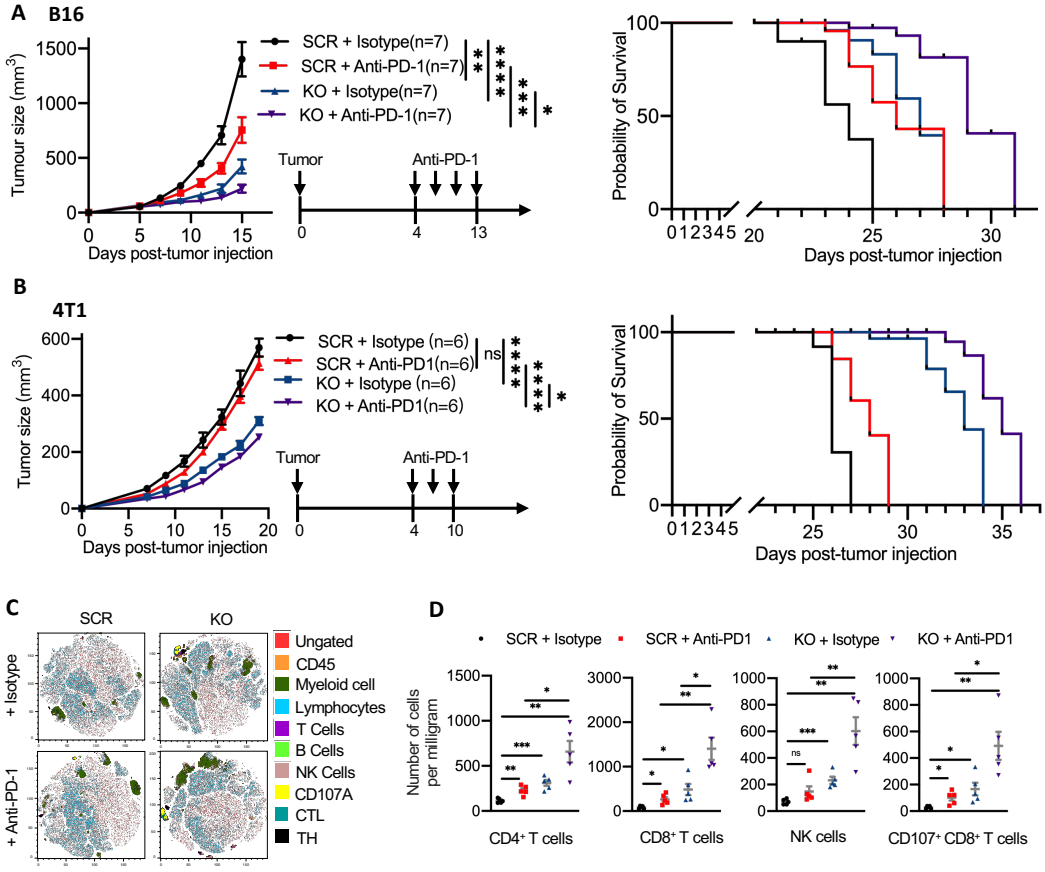

Fig. 3: Depletion of *Mettl5* increases the efficacy of tumor immunotherapy

A, Anti-PD-1 antibody was administered to *Mettl5*-KO and SCR B16-F10 tumor-bearing C57BL/6N mice on days 4, 7, 10, and 13 post-implantation, followed by longitudinal monitoring of tumor volume (left) and overall survival (right).

B, Anti-PD-1 antibody was administered to *Mettl5*-KO and SCR B16-F10 tumor-bearing Balb/c mice on days 4, 7, and 10 post-implantation, followed by longitudinal monitoring of tumor volume (left) and overall survival (right).

C, t-SNE analysis of immune cell populations in the tumor microenvironment of tumor in C57BL/6N mice. Mice were treated with either isotype control or anti-PD-1 antibody. The analysis includes the following immune cell populations: Lymphocytes, $CD45^+$ cells, Myeloid cells, T Cells, B Cells, NK Cells, $CD107a^+$ cells, CTL, and T Helper (TH) cells. The plots show the distribution of these immune cell populations in the tumor microenvironment for SCR and KO groups treated with isotype control or anti-PD-1 antibody.

1070 **D**, Quantitative analysis of immune cell populations in the tumor microenvironment of
1071 tumor in C57BL/6N mice. The number of $CD4^+$ T cells, $CD8^+$ T cells, NK cells, and
1072 $CD107a^+$ $CD8^+$ T cells per milligram of tumor tissue was determined by flow cytometry.
1073 **Note:** Mouse survival curves were plotted using endpoints: death or tumor volume
1074 exceeding 2000 mm^3. **A**, **B**, two-way ANOVA. Data were presented as mean ± SEM.
1075 **D**, Student's t-tests. Data were represented as mean ± SD (n=5). *P<0.05, **P<0.01,
1076 ***P<0.001, ****P<0.0001, ns: not significant.

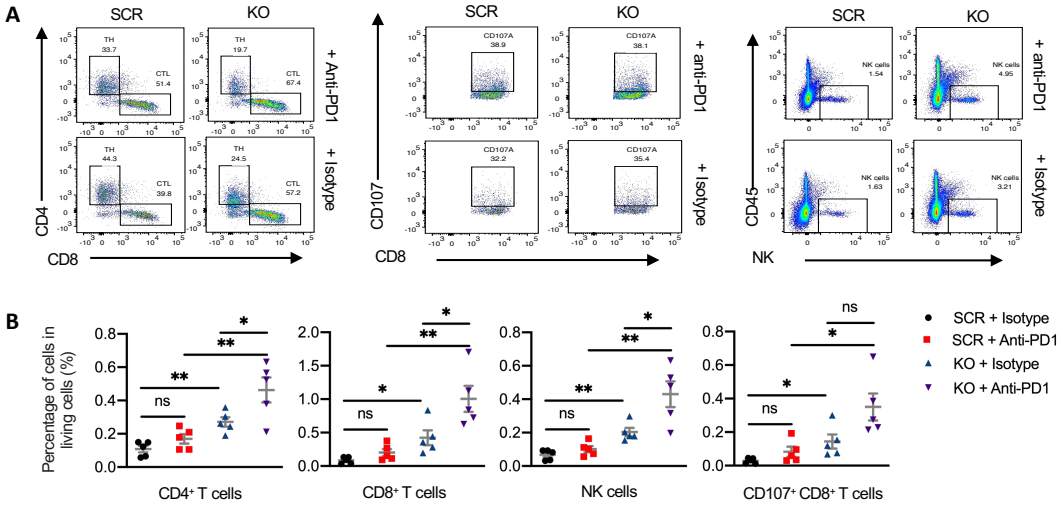

1077

1078 **Fig. S3: Depletion of *Mettl5* enhances intra-tumoral T-cell infiltration**

1079 **A**, **B**, Representative flow cytometry image (**A**) showing the distribution of $CD4^+$ T

1080 cells, $CD8^+$ T cells (left), $CD107a^+$ $CD8^+$ T cells (middle), and NK cells(right). The

1081 relative frequency of immune cells amongst living cells (**B**) were assessed.

1082 **Note: B**, Student's t-tests. Data were represented as mean ± SD (n=5). **P*<0.05,

1083 ***P*<0.01, ns: not significant.

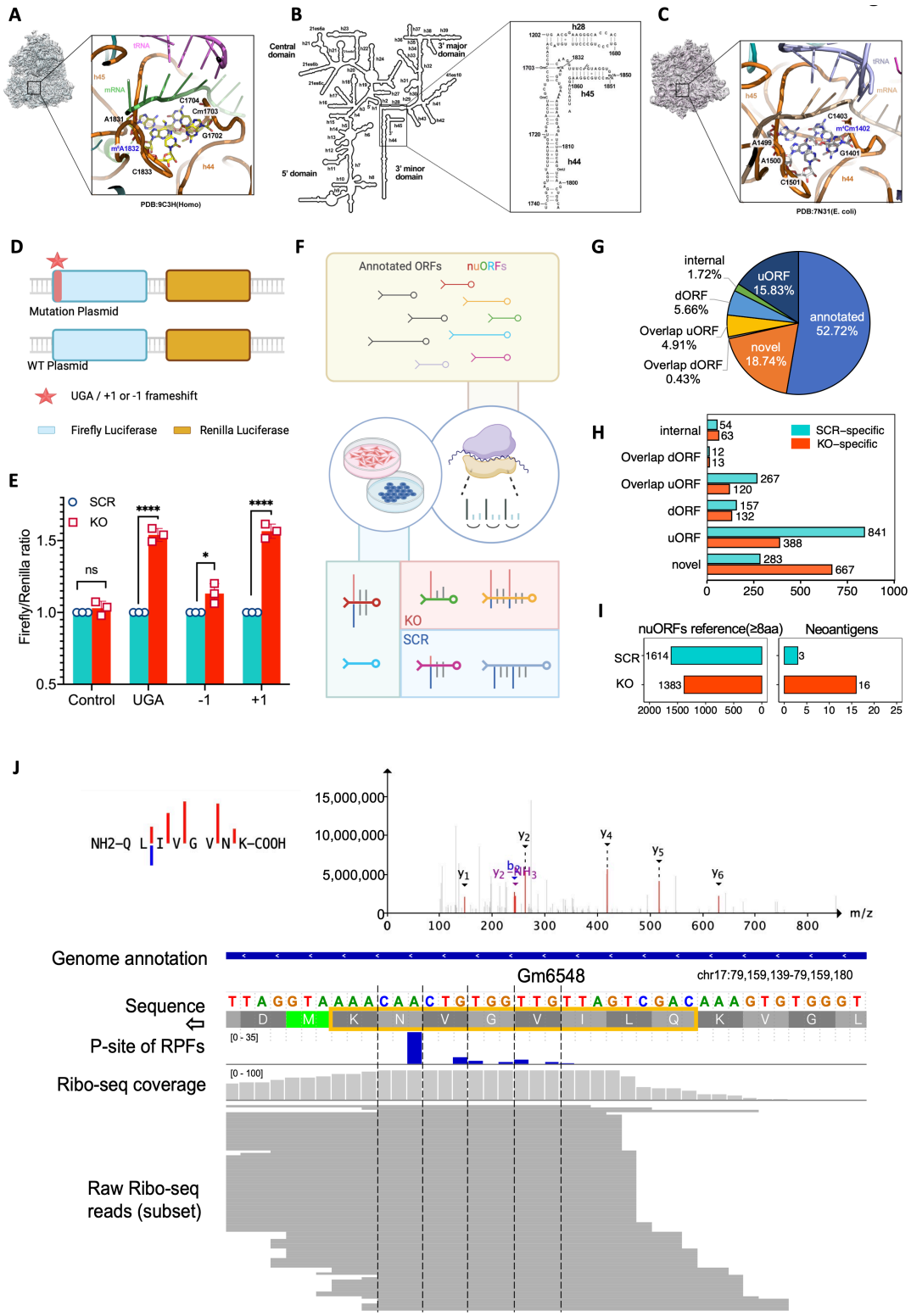

Fig. 4: Depletion of *Mettl5* induces neoantigen generation

A, Close-up view of the human 40S ribosomal subunit decoding center highlighting the m^{6}A1832 modification (blue).

B, Overall structure of 18S rRNA within the decoding center.

1089 **C**, Close-up of the *E. coli* 30S ribosomal subunit decoding center featuring the
1090 $m^4Cm1402$ modification (blue).
1091 **D**, Scheme of reporter vector. Dual-luciferase plasmid constructs were designed with a
1092 UGA stop codon, +1 frameshift, or -1 frameshift upstream of the firefly luciferase gene,
1093 with Renilla luciferase as an internal control.
1094 **E**, Translation efficiency of wildtype and mutant firefly luciferases in SCR and *Mettl5*
1095 KO cells was revealed by a reporter assay. Firefly luciferase activity was normalized to
1096 Renilla luciferase, with the SCR group set as the baseline (relative ratio = 1).
1097 **F**, Schematic workflow of generating nuORFdb v.1.0. ORFs from ribosome profiling
1098 (Ribo-seq) data were classified into annotated ORFs and novel ORFs (nuORFs), which
1099 were compiled as a database for subsequent analyses. For differential nuORF
1100 expression between *Mettl5*-KO and SCR groups, we classified nuORFs into three
1101 categories: (1) Shared nuORFs (expressed in both groups with <1.5-fold TPM
1102 difference), (2) *Mettl5*-KO-specific nuORFs (exclusive to *Mettl5*-KO or with ≥1.5-fold
1103 higher TPM than SCR), and (3) SCR-specific nuORFs (exclusive to SCR or with ≥1.5-
1104 fold higher TPM than *Mettl5*-KO).
1105 **G**, Pie chart illustrating the classification of nuORFs identified in *Mettl5*-KO and SCR
1106 group. The chart shows the percentage distribution of different nuORF categories
1107 relative to the total nuORFs.
1108 **H**, Differential analysis of nuORF categories between *Mettl5*-KO and SCR groups.
1109 **I**, Mass spectrometry-based identification of MHC-bound peptides in SCR and *Mettl5*-
1110 KO samples, nuORF-derived neoantigens were identified using corresponding nuORFs
1111 (>8 aa) as reference sequences.
1112 **J**, A representative neoantigen (NH2-Q-L-I-V-G-V-N-K-COOH) identified by MHC-
1113 I immunopeptidomics and Ribo-seq in *Mettl5*-KO tumors. The characteristic 3-
1114 nucleotide periodicity of ribosome-protected fragments confirmed its translational
1115 activity. Top panel: the mass spectra for the identified neoantigen; Bottom panel: Ribo-

1116 seq revealing nuORF reading frames. Blue bars, in-frame reads; LC-MS/MS-detected
1117 peptide was highlighted with a yellow box.
1118 **Note: E**, Student's t-tests. Data were represented as mean ± SD (n=3). *P<0.05,
1119 ****P<0.0001, ns: not significant.

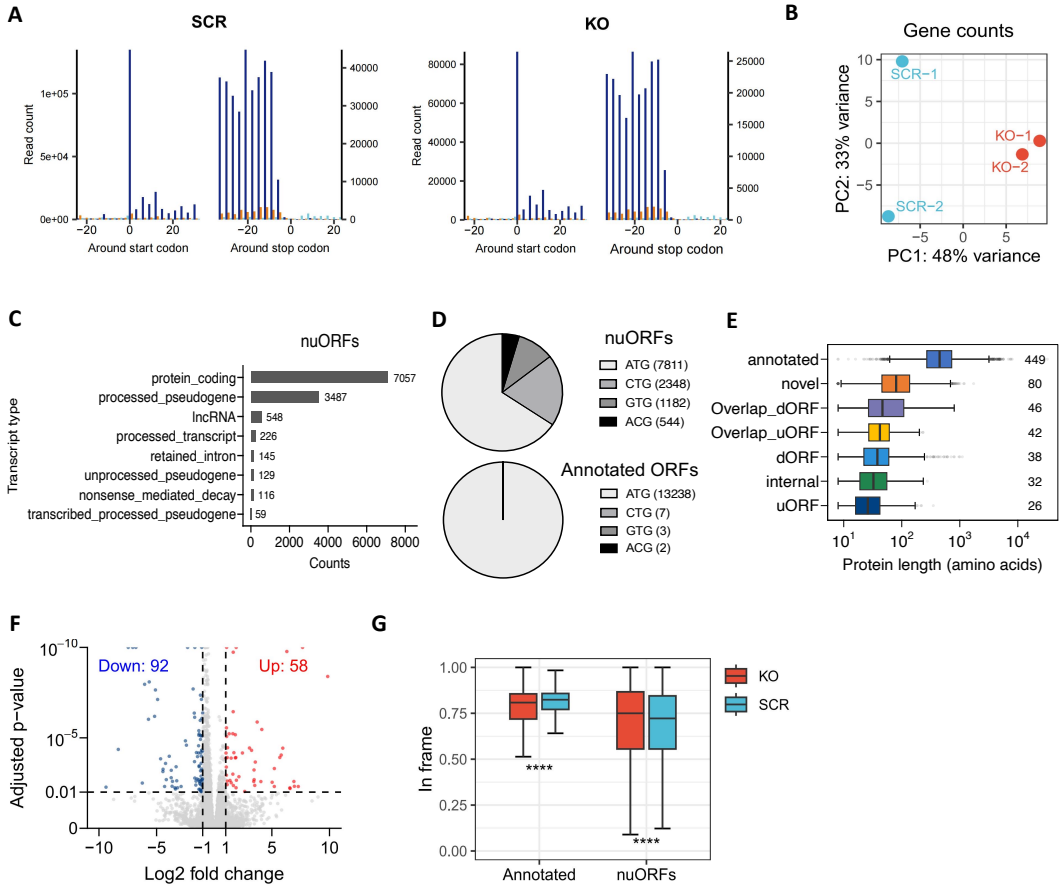

Fig. S4: Identification of novel ORFs induced by *Mettl5* deficiency

A, Quality control of Ribo-seq data in SCR (left) and *Mettl5* KO (right) cells.

B, The PCA plot shows the separation between *Mettl5*-KO and SCR groups based on gene counts

C, Distribution of transcript types for nuORFs identified by Ribo-seq.

D, Distribution of start codons for nuORFs and annotated ORFs in Mettl5-KO and SCR groups.

E, Protein length distribution (in amino acids) for different ORF categories in *Mettl5*-KO and SCR groups.

F, Volcano plot depicting down-regulated (blue) and up-regulated (red) genes identified by Ribo-seq in *Mettl5* KO cells compared with SCR cells.

G, Distribution of in-frame translation events in *Mettl5*-KO and SCR groups across annotated ORFs and nuORFs.

1134 **Note: G**, Student's t-tests. Data were presented as median (IQR 25-75%).

1135 ****P<0.0001.

1136

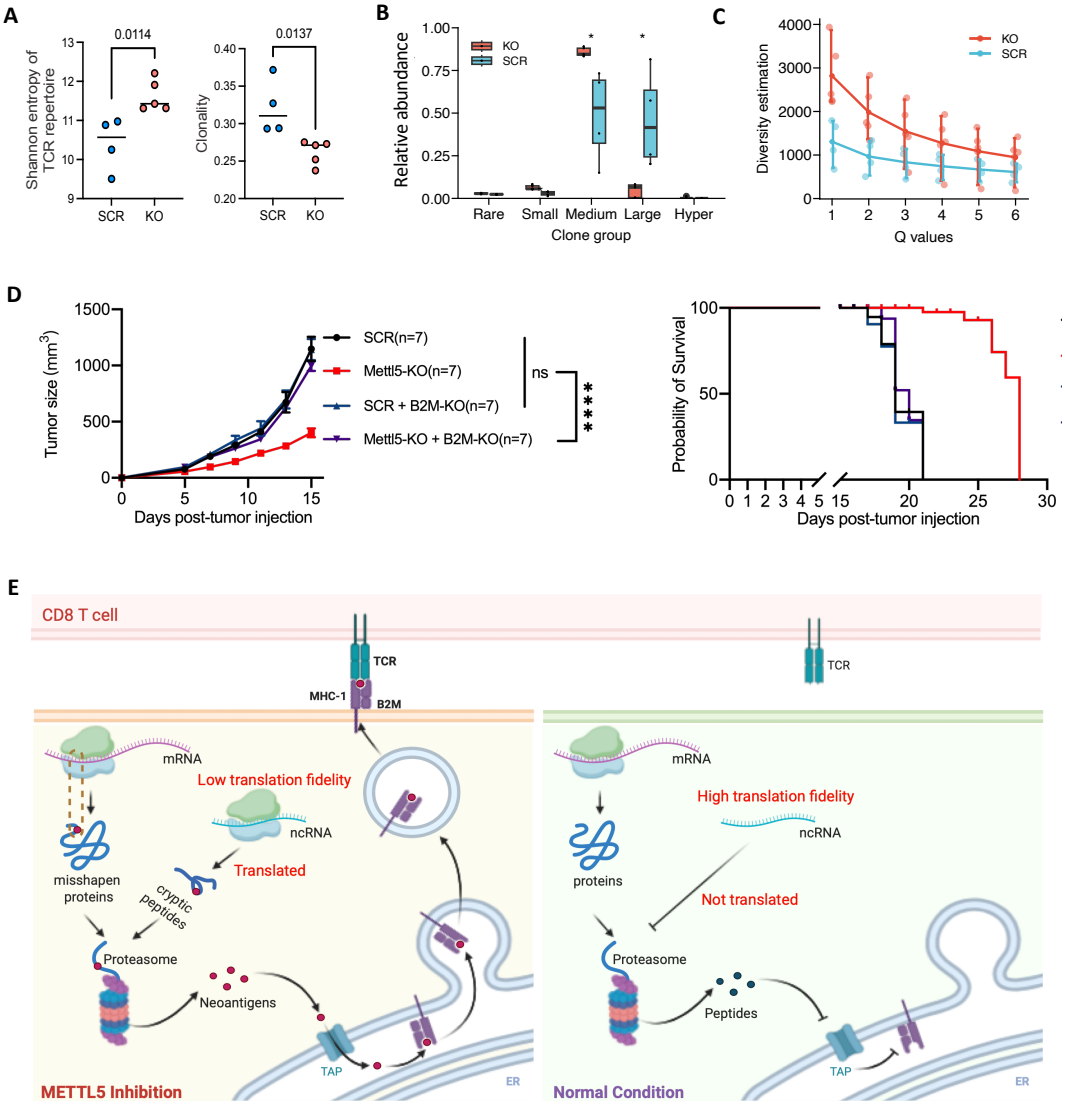

Fig. 5: Neoantigens are essential for the anti-tumour immune responses elicited by *Mettl5* depletion

A, Scatter plots depicting comparative distributions of TCR repertoire diversity (Shannon entropy) and clonality between *Mettl5*-KO and SCR groups.

B, Violin plots showing the distribution of clonal expansion levels in *Mettl5*-KO versus SCR groups, with clones categorized by abundance thresholds: Rare (<1e-05), Small (1e-04), Medium (0.001), Large (0.01), and Hyper-expanded (1).

C, Comparative diversity analysis (Hill numbers q=1–6) between *Mettl5*-KO and SCR groups.

1147 **D**, Growth curve of tumors in C57BL/6N mice subcutaneously implanted with SCR,
1148 *Mettl5*-KO, SCR plus *B2m*-KO, *Mettl5*-KO plus *B2m*-KO B16-F10 cells. The tumor
1149 growth (left) and overall survival (right) were compared.
1150 **E**, Working model for the critical role of METTL5 in tumor immunity through
1151 neoantigen generation. *Mettl5* deficiency abrogates m^6A deposition in the ribosomal
1152 decoding center, impairing ribosomal function and compromising translation fidelity.
1153 These defects lead to aberrant non-canonical translation events that generate
1154 immunogenic neoantigens, thereby stimulating anti-tumor immunity.
1155 **Note:** Mouse survival curves were plotted using endpoints: death or tumor volume
1156 exceeding 2000 mm^3. **A, B**, **D**, Student's t-tests. **A,** Data were represented as mean ±
1157 SD. **B**, Data were presented as median (IQR 25-75%). **D** Data were presented as mean
1158 ± SEM. *P<0.05, ****P<0.0001, ns: not significant.
1159

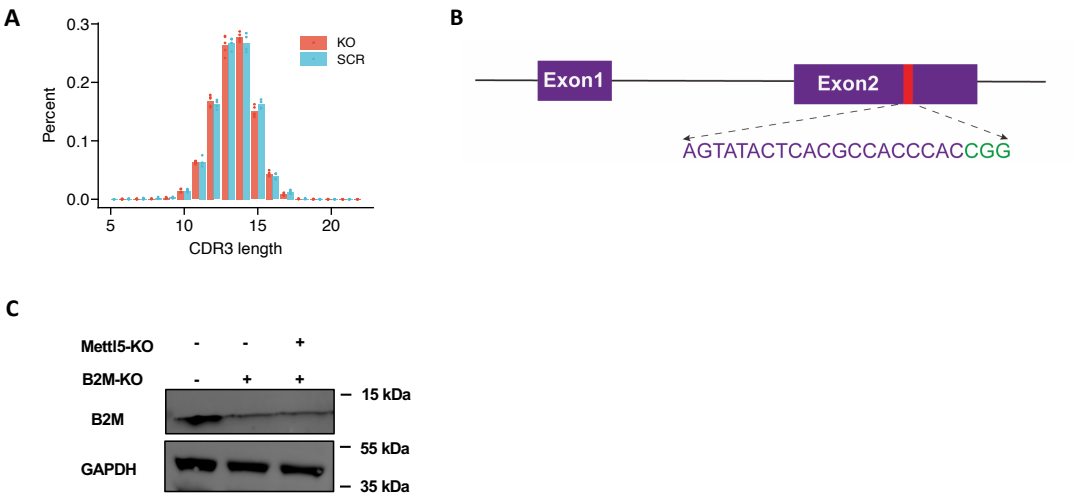

Fig. S5: TCR-seq QC and generation of *B2m* knockout cell lines

A, Scatter plot from TCR-seq quality control showing no significant differences in CDR3 length distribution between KO and SCR groups.

B, Schematic diagram of sgRNA targeting mouse *B2m* locus.

C, Western blotting confirmed the depletion of *B2m* in SCR and *Mettl5*-KO B16-F10 cells. GAPDH was used as internal control.

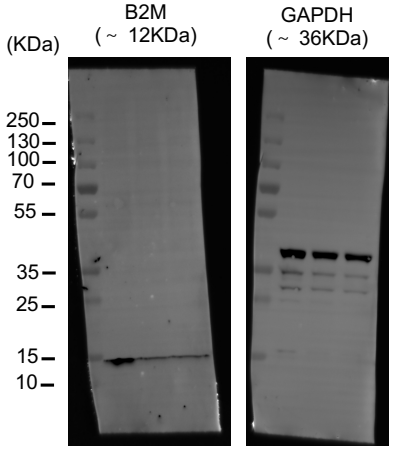

Fig. S6: Uncropped original Western blot images